Article

Vision 20/20: Magnetic resonance imaging-guided attenuation correction in PET/MRI: Challenges, solutions, and opportunities

MEHRANIAN, Abolfazl, ARABI, Hossein, ZAIDI, Habib

Abstract

Attenuation correction is an essential component of the long chain of data correction techniques required to achieve the full potential of quantitative positron emission tomography (PET) imaging. The development of combined PET/magnetic resonance imaging (MRI) systems mandated the widespread interest in developing novel strategies for deriving accurate attenuation maps with the aim to improve the quantitative accuracy of these emerging hybrid imaging systems. The attenuation map in PET/MRI should ideally be derived from anatomical MR images; however, MRI intensities reflect proton density and relaxation time properties of biological tissues rather than their electron density and photon attenuation properties. Therefore, in contrast to PET/computed tomography, there is a lack of standardized global mapping between the intensities of MRI signal and linear attenuation coefficients at 511 keV. Moreover, in standard MRI sequences, bones and lung tissues do not produce measurable signals owing to their low proton density and short transverse relaxation times. MR images are also inevitably subject to artifacts that degrade their [...]

Reference

MEHRANIAN, Abolfazl, ARABI, Hossein, ZAIDI, Habib. Vision 20/20: Magnetic resonance imaging-guided attenuation correction in PET/MRI: Challenges, solutions, and opportunities. *Medical physics*, 2016, vol. 43, no. 3, p. 1130-55

DOI : 10.1118/1.4941014
PMID : 26936700

Vision 20/20: Magnetic resonance imaging-guided attenuation correction in PET/MRI: Challenges, solutions, and opportunities

Abolfazl Mehranian and Hossein Arabi
Division of Nuclear Medicine and Molecular Imaging, Geneva University Hospital, Geneva CH-1211, Switzerland

Habib Zaidi[a)]
Division of Nuclear Medicine and Molecular Imaging, Geneva University Hospital, Geneva CH-1211, Switzerland; Geneva Neuroscience Centre, University of Geneva, Geneva CH-1205, Switzerland; and Department of Nuclear Medicine and Molecular Imaging, University of Groningen, Groningen 9700 RB, Netherlands

(Received 22 April 2015; revised 15 January 2016; accepted for publication 18 January 2016; published 8 February 2016)

Attenuation correction is an essential component of the long chain of data correction techniques required to achieve the full potential of quantitative positron emission tomography (PET) imaging. The development of combined PET/magnetic resonance imaging (MRI) systems mandated the widespread interest in developing novel strategies for deriving accurate attenuation maps with the aim to improve the quantitative accuracy of these emerging hybrid imaging systems. The attenuation map in PET/MRI should ideally be derived from anatomical MR images; however, MRI intensities reflect proton density and relaxation time properties of biological tissues rather than their electron density and photon attenuation properties. Therefore, in contrast to PET/computed tomography, there is a lack of standardized global mapping between the intensities of MRI signal and linear attenuation coefficients at 511 keV. Moreover, in standard MRI sequences, bones and lung tissues do not produce measurable signals owing to their low proton density and short transverse relaxation times. MR images are also inevitably subject to artifacts that degrade their quality, thus compromising their applicability for the task of attenuation correction in PET/MRI. MRI-guided attenuation correction strategies can be classified in three broad categories: (i) segmentation-based approaches, (ii) atlas-registration and machine learning methods, and (iii) emission/transmission-based approaches. This paper summarizes past and current state-of-the-art developments and latest advances in PET/MRI attenuation correction. The advantages and drawbacks of each approach for addressing the challenges of MR-based attenuation correction are comprehensively described. The opportunities brought by both MRI and PET imaging modalities for deriving accurate attenuation maps and improving PET quantification will be elaborated. Future prospects and potential clinical applications of these techniques and their integration in commercial systems will also be discussed. [http://dx.doi.org/10.1118/1.4941014]

Key words: PET/MRI, quantification, attenuation map, attenuation correction, tracer uptake

1. INTRODUCTION

Hybrid positron emission tomography/magnetic resonance imaging (PET/MRI) has emerged as a new imaging modality enabling concurrent morphological and molecular characterization of different organs/tissues and physiopathological conditions. Over the last decade, tremendous efforts have been directed toward addressing the challenges faced by PET/MRI systems from two perspectives: (i) instrumentation and conceptual system design and (ii) improvement of quantitative performance to achieve at least comparable accuracy to standard PET/computed tomography (CT) systems where CT-based attenuation correction (CTAC) is the standard procedure. With the advent of solid-state photodetectors, the challenge of mutual compatibility between PET and MRI subsystems has now been reasonably addressed, paving the way toward fully integrated clinical time-of-flight (TOF) PET/MR systems.[1–3] However, accurate attenuation correction (AC) of PET data has remained a major challenge in PET/MRI.[4,5] A number of active research groups have focused on the development of innovative techniques for deriving accurate attenuation maps to improve the quantitative accuracy of PET/MR imaging. During the last decade, significant progress has been achieved in this field as thoroughly appraised in previous reviews by Hofmann *et al.*,[6] Bezrukov *et al.*,[4] and many others.[7–9]

In this paper, we examine the challenges and recent technical advances in the rapidly evolving field of attenuation correction in PET/MRI. Overall, AC methods in PET/MRI can be categorized into three main classes: (i) segmentation-based approaches, which segment MR images into different tissue classes and assign predefined attenuation coefficients to each class, (ii) atlas-based and machine learning techniques in which a coregistered MR-CT atlas dataset is used to derive a pseudo-CT image and/or to learn a mapping function that predicts the pseudo-CT image from patient-specific

MR image, and (iii) the recently revisited emission- and transmission-based methods, in which the attenuation map is estimated from TOF emission or transmission data. We discuss the challenges and technical considerations involved for attenuation map generation in PET/MRI and provide a detailed overview of MRI-guided attenuation correction (MRAC) methods with special emphasize on their pros and cons. A possible scenario of future developments and opportunities is also provided.

In PET/MRI, the attenuation map at 511 keV should ideally be derived from the acquired MR images. However, contrary to x-ray CT, MRI signals are not correlated with electron density and photon attenuating properties of tissues, but rather to proton density and magnetic relaxation properties. Therefore, there is no unique global mapping technique to convert MRI intensities to attenuation coefficients. Similar to early transmission-based AC methods,[10] the most straightforward way to derive attenuation maps in PET/MRI is to classify MR images for segmentation of different tissue classes and assign proper linear attenuation coefficients (LACs) to each tissue class. However, lung tissues and cortical bones, which are two important tissue types in attenuation maps, exhibit low signals on images acquired using conventional MR pulse sequences. Therefore, the lungs, bones, and air pockets, which also produce a low MR signal intensity, cannot be well differentiated from each other for the generation of MRI segmentation-based attenuation maps. Ultrashort echo time (UTE) pulse sequences have also been investigated for the detection and visualization of bones[11,12] as well as lung parenchyma.[13] However, UTE MRI is prohibitively time-consuming and sensitive to magnetic field inhomogeneities and, as such, it is not yet clinically feasible for whole-body MRAC of PET data. However, substantial progress has been recently achieved in accelerated sub-Nyquist MRI acquisitions using parallel MRI (pMRI) and compressed sensing (CS) techniques, which are particularly suited for UTE data acquisition.[14,15]

In contrast to PET/CT, in whole-body PET/MRI scans, the arms are positioned down mainly because of patient comfort and support as well as coil positioning constraints. However, the limited transaxial field-of-view (FOV) of MRI scanners (45–50 cm) can result in the truncation of the arms and shoulders in the acquired MRI images[16] compared to the larger useful transaxial FOV of PET scanners (60–70 cm). The generation of attenuation maps from truncated MR images is another challenge in terms of deriving complete attenuation maps in whole-body scans. In patients with metallic implants, such as titanium prosthesis or dental fillings, the main magnetic field around the implants is usually locally distorted producing expansive signal voids with peripheral areas of high intensity known as blooming or magnetic susceptibility artifacts.[17] These artifacts are more pronounced in fast GRE MRI sequences, often used for MRAC, due to the lack of 180° refocusing radio frequency (RF) pulses. The void artifacts can be mis-segmented or lead to inaccurate LAC prediction by atlas-based learning techniques.

A further challenge arises from the attenuation and scattering of annihilation photons by MRI RF coils in integrated or insert-based PET/MRI systems as well as other attenuating objects present in the PET FOV including patient's bed and patient positioning aids. In whole-body MRI imaging, integrated body coils are usually used for receiving MRI signals. Moreover, to improve signal-to-noise ratio, without compromising acquisition time, flexible surface RF coils or head and neck coils are employed during scanning. Similar to bony structures, short T2 materials do not provide measurable signals in conventional MRI sequences and therefore remain invisible. The presence of such attenuating material, especially flexible coils that can be placed in arbitrary positions and orientations, can locally affect PET quantification and must therefore be included in the attenuation map. Several other challenges and problems specific to each category of MRAC methods are discussed in Sec. 3 together with recent advances in the field.

2. STRATEGIES FOR MRI-GUIDED ATTENUATION CORRECTION IN PET/MRI

In this section, a comprehensive overview of the outlined AC strategies is elaborated with special emphasize on current state-of-the art techniques. For the sake of completeness, earlier contributions discussed in previous reviews are also briefly covered. Table I summarizes the major contributions for each category of methods highlighting the working principles and required data for implementation, major advantages and findings, limitations, performance, and reported quantitative accuracy.

2.A. Segmentation-based methods

The attenuating tissues in the body consist mainly of soft tissues, adipose (fat) tissue, lungs, air cavities (sinuses, abdominal air pockets), and cortical and spongy bones. Each tissue class has different intra/interpatient attenuation coefficients at 511 keV as summarized in Table II. In segmentation-based MRAC methods, the aim is to segment MR images into (at least) the above-mentioned six tissue classes[18] and to assign representative, or if possible, patient-specific, linear attenuation coefficients to each tissue class.

2.A.1. Brain imaging

In brain PET imaging, the cortical bones of skull substantially contribute to the attenuation and scattering of annihilation photons. For accurate PET quantification, the bones must, therefore, be accounted in the MRAC map. Otherwise if substituted by soft tissue, the tracer uptake might be underestimated by up to 25% in cortical regions and 5%–10% in central regions of the cranium, as recently reported by Anderson *et al.*[19] In a comparative study, Teuho *et al.*[20] also reported the largest underestimations 11%–17% in the temporal cortex and orbito-frontal cortex by ignoring the bones.

One of the earliest segmentation-based MRAC studies was reported by Zaidi *et al.*,[21] where T1-weighted MR images were

Table I. Overview of MRI-guided attenuation correction strategies in PET/MRI.

Category	Body region	Technique and data	Tissue classes (attenuation values)	Key advantages of the method/findings of study	Limitations	Quantification errors
Segmentation-based methods (Sec. 2.A)	Brain	Segmentation of T1W MRI using supervised fuzzy C-means clustering (Ref. 21)	Brain tissue (0.099 cm^{-1}), skull (0.14 cm^{-1}), nasal sinuses (0.054 cm^{-1}), and air (0 cm^{-1})	Inclusion of bones	Semiautomatic segmentation of bones	2.4% bias using ten patients in comparison to transmission μ-maps
		Neural network-based segmentation of MP-RAGE MRI (Refs. 22 and 24)	Air (0 cm^{-1}), brain tissue (0.096 cm^{-1}), skull (0.146 cm^{-1}), and Mastoid process (0.054 cm^{-1})	Fully automatic, knowledge-based	Mis- or oversegmentation of bones in the presence of abnormal anatomy or pathology	−6.1% to 2.7% bias in cortical regions and −7.0% to 5.6% for subcortical regions using four patients
		Segmentation of dual-echo UTE MRI using region-growing and thresholding (Ref. 12)	Air (0 cm^{-1}), soft tissue (0.096 cm^{-1}), and bones (0.12 cm^{-1})	Direct segmentation of bones	Long acquisition time (6 min), mis-segmentation at air–tissue interfaces	Average 5% error in brain tissues of five PET/CT/MRI patients
		Segmentation of dual-echo UTE MRI using morphological closing and arithmetical operations (Ref. 11)	Air (0 cm^{-1}), soft tissue (0.096 cm^{-1}), and bones (0.136 to 0.180 cm^{-1})	Direct segmentation of bones, 3.3 min acquisition time	Poor spatial resolution of UTE data, mis-segmentation at air–tissue interfaces	Bone LACs of 0.143 and 0.151 cm^{-1} resulted in best bias variability trade-off in quantification
		Segmentation of triple-echo UTE MRI using thresholding and morphological filtering (Ref. 25)	Air (0 cm^{-1}), soft tissue (0.1 cm^{-1}), fat (0.09 cm^{-1}), and bones (0.172 cm^{-1})	Direct segmentation of bones and inclusion of fat	Bone misclassifications at paranasal sinuses	Over 80% of bone voxels were correctly classified in six studied patients
		Segmentation of Dixon fat and water MRI (Ref. 19)	Air, soft-tissue fat	Radial variation of quantification errors when bones are ignored	Presence of metal-induced artifacts in MRAC maps	SUV bias of 25% in cortical regions and 5%–10% in central regions of the brain (19 patients)
	Whole-body	Segmentation of 3D T1 SPGR MRI using deformable shape modeling and thresholding (Ref. 16)	Air, lungs, and soft tissue	Fast, fully automatic	Bone/air and lung segmentation challenging, truncation artifacts, etc.	<10% SUV bias in malignant soft-tissue lesions with respect to CTAC, −12% bias in a pelvis lesion (15 patients)
		Segmentation of two-point Dixon MRI (Ref. 26)	Air, lungs, and soft and fat tissues	Inclusion of fat tissue, fast	Same as above	−8% SUV bias in bone lesions (35 patients)
		Phase-field-based segmentation and mapping of two-point Dixon MRI (Ref. 27)	Continuous fat/water (0.086-0.1 cm^{-1}), lungs, and air	Continuous fat and water LACs	Same as above	Mean SUV bias of 10% in the liver and −2% in malignant lesions (16 patients)
Atlas-based segmentation, registration and machine learning methods (Sec. 2.B)	Brain (without UTE)	Patch-based Gaussian process regression and atlas registration (Ref. 28)	Continuous	Robust to misregistration errors	Very time-consuming (Gaussian process regression)	Mean SUV bias of 3% for predefined regions of interest with respect to CTAC

TABLE I. (*Continued*).

Category	Body region	Technique and data	Tissue classes (attenuation values)	Key advantages of the method/findings of study	Limitations	Quantification errors
		Voxelwise classification of air/bone from MRI without atlas registration using random forest method (Ref. 29)	Binary	No need for atlas registration, time efficient	Susceptible to presence of artifacts in MR image	Dice values of 0.83 ± 0.08 and 0.98 ± 0.01 for air and bone, respectively
		Voxelwise atlas fusion using LNCC as image similarity measure (Ref. 30)	Continuous	Very robust to misregistration errors	Time-consuming (40 atlas registrations are required)	Relative absolute error of 5% for the full head with respect to CTAC
		Patch-based pseudo-CT generation without using deformable atlas registrations (Ref. 31)	Continuous	No need for atlas registration, time efficient	—	Dice values of 0.84 ± 0.02 for bone volume
	Brain (with UTE)	Pseudo-CT generation by including spatial information into Gaussian mixture regression (Ref. 32)	Continuous	Robust pseudo-CT generation using UTE sequence	Requires four UTE images with different echo times and flip angles	Mean absolute prediction deviation of 130 ± 18 HU with spatial information
		Patient-specific bone attenuation coefficient estimation based on UTE (Please check, and correct if necessary.Ref. 33)	Continuous bone, air (0 cm^{-1}), fat (0.092 cm^{-1}), and soft-tissue (0.1 cm^{-1})	Patient-specific bone attenuation coefficient	Requiring UTE and Dixon sequences	Dice values of 0.75 ± 0.05 across 98 subjects for bone and 0.60 ± 0.08 for sinus air cavities
		Patch-based pseudo-CT generation via Bayesian framework (Ref. 34)	Continuous	No atlas registration and segmentation required	—	PET pseudo-CT AC exhibited correlation coefficient of 0.99 with respect to PET-CTAC
	Whole-body	Gaussian process regression and atlas registration (Ref. 35)	Continuous	Robust to misregistration errors	High computational time	In regions of normal physiologic uptake, the average bias was $8\% \pm 8\%$ and for lesions was $6\% \pm 5\%$
		Gaussian process regression and tissue segmentation (Ref. 36)	Continuous bone, lung (0.024 cm^{-1}), fat (0.0856 cm^{-1}), nonfat (0.1007 cm^{-1}), and Fat/soft-tissue mixture (0.0988 cm^{-1})	Robust to metal induced artifact in MR images	—	SUV bias of $24\% \pm 6\%$ for lesions near bone and $0.6 \pm 11.1\%$ for lesions affected by MR susceptibility artifacts
		Most similar single atlas registration (Ref. 37)	Continuous	Very time efficient (only one atlas registration)	Lack of multiatlas consensus	SUV bias in bony regions ranging from -3% to 4% and -2.1% to 2.6% for lean tissue
		Improved Gaussian process regression with sorted atlas registration (Ref. 38)	Continuous	Very robust to misregistration errors, patient-specific lung LACs	High computational time	Up to 4% lung SUV bias (14 patients)

Table I. (*Continued*).

Category	Body region	Technique and data	Tissue classes (attenuation values)	Key advantages of the method/findings of study	Limitations	Quantification errors
Emission- and transmission-based methods (Sec. 2.C)		Attenuation estimation using consistency conditions of TOF Radon transform (Ref. 39)	Continuous	Estimation of attenuation sinogram and analytical reconstruction	ACFs are determined up to a constant scaling factor	—
		Maximum likelihood reconstruction of attenuation and activity (MLAA) only TOF EM data (Ref. 40)	Continuous	Patient-specific LACs	Estimated LACs should be corrected for a missing scale factor	—
		MRI-guided MLAA using anatomical regions (Ref. 41)	Discrete LACs (depending on the number of MR regions)	Reduced noise and cross talks in estimated mu maps	Unsolved scale factor, MRI mis-segmentation errors, limited tissue heterogeneity	Bias of −6% in the lungs, −10% in bones, −3% in soft tissues (only one patient)
	Whole-body	MLAA using MR-constrained Gaussian mixture models (Ref. 42)	Continuous, mean LACs of lungs, fat, soft tissue, and bones: 0.027, 0.086, 0.097, 0.104 cm^{-1}	Solved the scale problem, robust to MRI-segmentation errors	Selection of regularization parameters, registration of a bone probability map	Bias of −4% in the lungs, −10% in bones, and −5.0% in soft tissues/lesions (five patients)
		Attenuation estimation from transmission data acquired in simultaneous transmission and TOF PET scanning (Ref. 43)	Continuous, mean LACs of lungs and soft tissue: 0.019 and 0.098 cm^{-1}, respectively	Patient-specific LACs with simultaneous transmission and emission scanning	External transmission source is required, imperfect separation of transmission and emission data results in scaling the LACs, increased radiation dose	~10% in the lungs and soft tissues and ~15% in bones (five patients)
		Attenuation estimation from transmission and emission (Ref. 44)	Continuous	Solved the scale problem and improved performance	External transmission source is required, increased radiation dose	—

TABLE II. Attenuation coefficients at 511-keV of different biological tissues (Ref. 7).

Tissue	Linear attenuation coefficient (cm^{-1})
Lung	0.018–0.03
Adipose tissue	0.086–0.093
Soft tissue	0.094–0.100
Spongious bone	0.110
Cortical bone	0.130–0.172

segmented into air, brain tissue, skull, and nasal sinuses using a supervised fuzzy C-means clustering. Later, Wagenknecht *et al.*[22,23] proposed an automatic tissue segmentation approach using neural network and prior knowledge about brain's anatomical regions. MR segmented regions showed a high correspondence with the CT segmented regions; however, the authors reported that this technique might result into mis- or oversegmentation of bones in the presence of abnormal anatomy or pathology. Since 2010, UTE MRI-based methods were then explored for bone visualization and direct segmentation of bones in brain studies. Catana *et al.*[11] and Keereman *et al.*[12] independently proposed a dual-echo UTE MRI sequence to derive three-class attenuation maps including air, soft tissue, and bones. Despite the promising results, the authors showed that UTE-based bone classification is still subject to over- or undersegmentation of bones, especially at bone/air or soft-tissue air interfaces due to diamagnetic susceptibility effects.

The combination of UTE and Dixon sequences for bone detection and fat separation in order to generate a four-class PET attenuation map was proposed by Berker *et al.*[25] The resulting four-class attenuation maps exhibited a high visual similarity to reference CTAC maps and over 80% of voxels in six studied patients were correctly classified. Using a trimodality PET/CT-MR system, Delso *et al.*[45] recently reported that the UTE segmented bones produce an acceptable overlap with reference CT bones over the skull; however, segmentation errors increase at the base of the skull, air interfaces eyeballs, and dental arch mainly due to susceptibility and motion effects. They concluded that bone segmentation errors can degrade the reconstructed PET images. Overall, postprocessing and segmentation procedures are required for bone extraction in UTE-based approaches, leading to significant differences in the obtained results.

2.A.2. Whole-body imaging

Contrary to brain imaging, bone segmentation in whole-body imaging is more challenging, especially the vertebra where the bones are spongy and contain tissues with a moderate MR intensity. The application of UTE MRI sequences for whole-body bone segmentation is not feasible yet since it is time-consuming for routine clinical usage, as a typical five to seven bed-position whole-body scan would take from 30 to 45 min.[12,46]

Current whole-body MRAC methods rely on the segmentation of MR images into three- or four-tissue classes, where bones are substituted by soft tissue. In earlier works, Hu *et al.*[16,47] and Schulz *et al.*,[48] implemented a three-class attenuation map on the Ingenuity TF PET/MR system[49] by segmenting MR images of a 3-min 3D T1-weighted gradient/spin-echo sequences into background air, lungs, and soft tissue. The clinical assessment of this technique indicated an overall underestimation of tracer uptake by up to 10% in malignant lesions,[16] while an overall bias of <7% in most malignant lesions was reported.[48] To include fat as fourth tissue class, Martinez-Möller *et al.*[26] used a Dixon sequence for the separation of fat and water. In their study, a mean standardized uptake value (SUV) error of about −8% was found for bone lesions compared to reference CTAC PET images. Hence, the authors concluded that this SUV bias is clinically irrelevant. In a follow-up study, Eiber *et al.*[50] also demonstrated that there is no statistically significant difference between PET/MRI and PET/CT for the anatomical localization of PET positive lesions. A mixture of fat and soft tissues was investigated by Hofmann *et al.*[35] as an additional tissue class, leading to mean absolute SUV errors of 8% and 14% in lesions and regions of normal uptake, respectively. In the same spirit, Wollenweber *et al.*[27] recently proposed a continuous fat/water (CFW) method allowing for continuous variation of fat and soft attenuation coefficients in the range of 0.086–0.1 cm^{-1}. Their quantitative analysis showed that the CFW and four discrete-class MRAC methods result in mean SUV errors of 10.4% and 5.7% in the liver and 1.7% and −1.6% in malignant lesions, respectively.

To evaluate the importance of bones in whole-body MRAC maps, as the fifth tissue class (in addition to air, lung, fat, and soft-tissue classes), Hofmann *et al.*[35] substituted bones in CTAC maps of 11 PET/CT patients by soft tissue. Their results demonstrated that the substitution of bones with soft tissue results in mean SUV errors of 4% in soft tissues adjacent to bones and 3% in soft-tissue lesions. A similar study was conducted by Samarin *et al.*[51] showing an underestimation of tracer uptake by 11% and 3% in osseous and soft-tissue lesions adjacent to bones, respectively. Aznar *et al.* also showed that the assignment of spongeous bone LACs (0.13 cm^{-1}) to all bones resulted in <5% quantification bias in soft tissue and bone lesions.[52] For sclerotic and osteolytic spine lesions, mean SUV underestimations of 16% and 7%, respectively, were reported.

Ouyang *et al.*[53] assessed PET quantification accuracy of three-, four-, and five-tissue class MRAC methods using PET/CT datasets and demonstrated that as the number of tissue classes increases, absolute quantification errors in different tissue classes, except the lungs, decrease. Using Monte Carlo simulation studies, Keereman *et al.*[9,18] also concluded that at least six-tissue classes (air, lung, soft tissue, fat, spongious, and cortical bones) should be identified in MRAC maps to reduce quantification errors to less than 5%. Similarly, Akbarzadeh *et al.*[54] confirmed that the accuracy of segmentation-based MRAC improves as the number of tissue classes increases.

Accurate segmentation of different tissue classes is also of high importance, especially in the presence of noise and

partial volume effect in clinical MR images. Keereman *et al.*[18] evaluated the effect of errors in the segmentation of lungs and cortical bones due to high level of noise and partial volume effect. They found that up to 20% misclassification of bone as soft tissue or 10% misclassification of lung as air yielded errors below 5%. It has also been reported that the mis-segmentation of air cavities in the head[55] and soft tissue in the abdomen[56] can noticeably affect the visual interpretation of PET images. Catana *et al.*[11] reported that substituting internal air cavities with soft tissue can introduce large overestimations (>20%) in adjacent structures. Choi *et al.*[57] showed that the mis-segmentation of brain ventricles as air in the three-class UTE-based MRAC maps resulted in significant underestimation of binding potential ratio in 16 patients suspected to have Parkinson disease. More recently, Brendle *et al.*[58] evaluated the frequency and impact of tissue misclassifications, caused by MR image artifacts on PET quantification and interpretation. An analysis of 100 PET/MRI studies revealed 276 identified artifacts affecting 21% of PET-avid lesions located mostly around metal implants (16%), in the lungs (19%), and outer body contours (31%). The quantitative analysis showed that attenuation artifacts led to significant SUV changes in areas with misclassification of air as soft tissue (i.e., metal artifacts) and soft tissue as lung. Ladefoged *et al.*[59] showed that inpainting regions misclassified as air, owing to the presence metal artifacts, with soft tissue increased mean and maximum SUVs averaged in the corrected regions across all patients by $52\% \pm 11\%$ and $28\% \pm 11\%$, respectively.

2.A.3. Segmentation of nonattenuation corrected (NAC) PET images

The segmentation of NAC PET images has also been revisited in the context of PET/MRI.[60] Chang *et al.*,[61] proposed a semiautomated iterative PET segmentation method for whole-body ^{18}F-FDG imaging to identify three tissue classes (i.e., background air, lung, and soft tissues). However, tissue classification from NAC PET images is generally limited to radiotracers that distribute throughout the body, such as ^{18}F-FDG, and probably will not work for specific (non-FDG) PET tracers. These techniques have been extensively employed to reduce truncation and metal artifacts in MRI-derived attenuation maps, as discussed in Secs. 3.A and 3.B.

2.B. Atlas-based segmentation, registration, and machine learning methods

To predict attenuation coefficients on a continuous scale or segment bone tissue class, current methods rely on either a number of atlases or template registration to the target subject or the use of machine learning techniques to train a classifier or mapping function to segment MR images or convert them into pseudo-CT images. An appraisal of the different atlas-based approaches with special emphasis on latest developments and advances in brain and whole-body imaging is given below.

2.B.1. Atlas-based and machine learning methods in brain imaging

Template-based attenuation map generation is commonly performed through nonlinear warping of a template of normal subjects to the target patient.[62] Templates are usually created by taking the average of multiple coregistered brain attenuation maps to represent mean attenuation coefficients and anatomical variability in a given population.[63] Wollenweber *et al.*[64] evaluated the performance of template-based AC compared to three-class segmentation-based method in head imaging and concluded that template-based AC provides adequate PET quantification compared to methods that do not account for bone.

Template-based approaches rely on a single anatomical template transformation which may suffer from registration errors or interpatient anatomical variability. The concept of utilizing consensus on multiple atlas registration helps to minimize nonsystematic registration errors. Hofmann *et al.*[28] proposed a method combining prior knowledge available in the multiple aligned atlas dataset with pattern recognition to generate patient-specific attenuation maps in brain imaging. A Gaussian process regression (GPR) is utilized to predict the substituted CT value for each voxel based on robust measurement of intensity similarity and spatial closeness of patches of voxels between the target image and atlas dataset and thus to minimize the impact of misregistration. Basically, methods relying on multiple atlas alignment outperform template-based or single atlas alignment methods owing to the uncorrelated error cancelation and power of consensus on multiple aligned atlases.[65,66]

In a comparative study, Uh *et al.*[65] demonstrated that the method proposed by Hofmann[28] may not be able to provide significant improvement compared to other atlas methods, such as arithmetic average of aligned CT atlas images, questioning its relevance given its high computation time (~271 min for a single study). To increase the robustness of atlas-based methods to misregistration errors, Burgos *et al.*[30] developed synthetic CTs through a multiatlas information propagation scheme for brain imaging where the MRI-derived patient's morphology is locally matched to the aligned dataset of MRI-CT pairs using a robust local image similarity measure based on local normalized cross-correlation (LNCC) criterion. The local matching through morphological similarity enables the algorithm to find local matches and similar anatomy across the atlas dataset. Using CT images as reference, the obtained pseudo-CT images were compared to a segmentation-based method using an UTE MRI sequence and to a simplified atlas-based method resulting in mean relative errors of 0.2%, −11.8%, and 0.8%, respectively. Examples of ground truth CT, proposed pseudo-CT, best-atlas CT,[30] UTE CT, and difference images are presented in Fig. 1.

Izquierdo-Garcia *et al.*[67] presented an approach for AC of brain PET data using statistical parametric mapping 8 (SPM8) software taking advantage of both segmentation and atlas-derived features. Anatomic MR images of 15 subjects were first segmented into six distinct tissue classes, and then nonrigidly coregistered using a diffeomorphic approach to

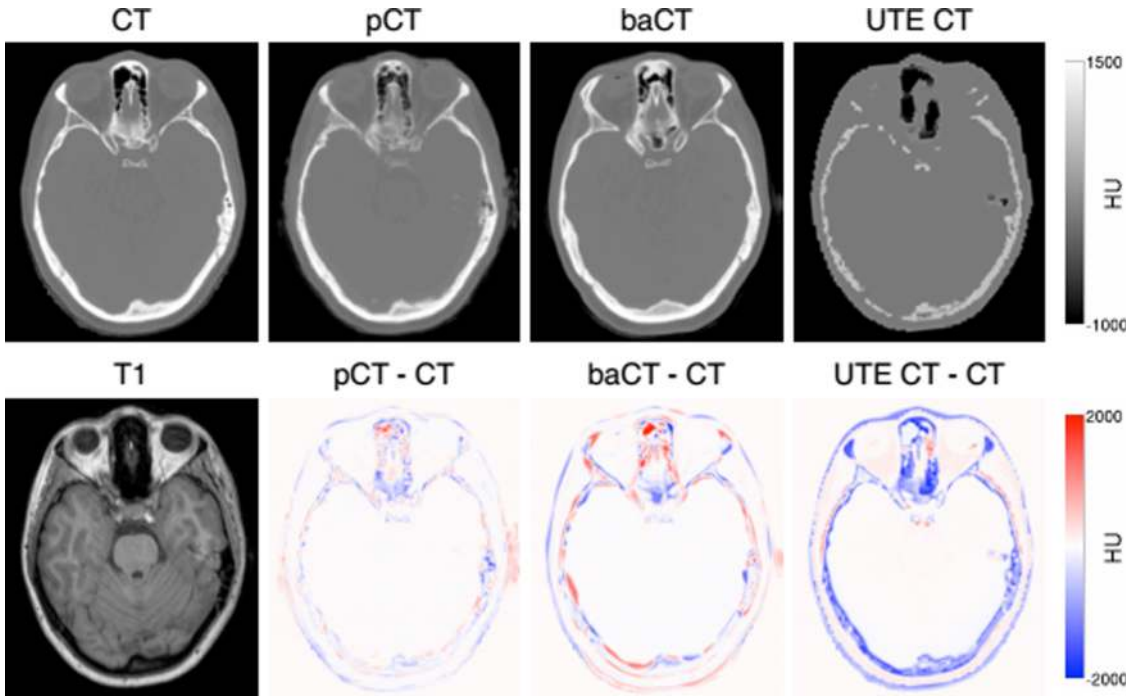

FIG. 1. Top row (from left to right): the acquired CT, the pseudo-CT generated by the proposed method, the best atlas CT (baCT), and the UTE CT. Bottom row (from left to right): the acquired T1, the difference between pCT and CT, the difference between baCT and CT, and the difference between UTE CT and CT. Reprinted with permission from Burgos *et al.*, "Attenuation correction synthesis for hybrid PET-MR scanners: Application to brain studies," IEEE Trans. Med. Imaging **33**(12), 2332–2341 (2014). Copyright 2014 by Creative Commons.

generate a MR-CT pair template. Thereafter, for a given subject, a similar procedure is carried out to coregister the target MR image to the template and the pseudo-CT image is constructed by applying the inverse transformations. In fact, the incorporated segmentation part enriched by the available information in MR images allows for a more accurate registration outcome. The quantitative analysis of the corresponding reconstructed PET images revealed mean relative errors of $3.9\% \pm 5.0\%$ and $2.7\% \pm 2.3\%$ for voxelwise and region of interest-based analysis, respectively.

To generate head attenuation maps for PET AC without using atlas registration or head template, Chan *et al.*[29] proposed a voxelwise classification method for bone/air segmentation from MR images using random forest classifier fed by a bag of features, such as gradient and local image context extracted from structural MR and uncorrected PET images. The same idea was evaluated by Yang *et al.*[68] utilizing conditional random field and image fusion based on dual-tree complex wavelet transform and extracted features from uncorrected PET and T1-weighted MR image. These methods were developed to eliminate the atlas registration step from the process of pseudo-CT generation to save computation time. However, a comparative study enabling to evaluate the performance of these methods against conventional atlas-based approaches is lacking.

In the context of PET/MRI-guided radiation therapy planning, Sjölund *et al.*[69] developed a surrogate CT generation approach using a deformable registration algorithm, known as the Morphon, enhanced with a certainty mask enabling to tailor the influence of certain regions in the registration. Furthermore, for the atlas fusion part, the collection of deformed atlas CTs is iteratively registered to their joint mean to build a more similar pseudo-CT to the target CT. Andreasen *et al.*[31] proposed a patch-based pseudo-CT generation approach using T1-weighted MR images without using deformable atlas registrations. In this method, a database is created with patches of voxels extracted from MR images together with their corresponding Hounsfield unit values from aligned CT images. Given an MR image, patches of voxels are extracted and compared to the database patches based on MR intensity similarity. A comparison between the proposed method and Gaussian mixture regression based on dual UTE scans[70] and multiatlas information propagation using T1-weighted scans[30,71] demonstrated a competitive performance and promising potential for use in MRI-only or PET/MRI-guided radiation therapy planning of brain malignancies.

2.B.2. UTE machine learning and atlas-based segmentation in brain imaging

The capability of UTE sequences to provide additional information to ease the detection of bones along with machine learning techniques to classify new observations can potentially yield promising results in terms of attenuation map determination for brain imaging. Johansson *et al.*[70] developed a Gaussian mixture regression algorithm trained with features derived from two UTE sequences and spatial information on a voxel-by-voxel basis to predict continuous LACs of the head.[32] They concluded that the inclusion of spatial information enhanced the accuracy of the estimated

pseudo-CT, particularly in small complicated anatomical regions, such as the inner ear and postnasal cavities. Ribeiro *et al.*[72] developed a feed forward neural network algorithm to predict nonlinearly the attenuation coefficients based on patches of voxels extracted from two UTE sequences and a template-based AC map of ten transmission PET scans.

In brain imaging, UTE MRI segmentation is subject to artifacts and under- or oversegmentation of bones.[45] The high level of noise and weak bone signal (low signal to noise ratio) are the main drawbacks of UTE imaging. To address this issue, many researchers used complimentary information present in an atlas or template. Poynton *et al.*[73] employed a probabilistic air/soft-tissue/bone atlas from T1-weighted, dual-echo UTE and coregistered CT images of 13 patients used to train a classifier that calculates the posterior class probability of each tissue class. The results showed an improvement over UTE-based segmentation, especially in the sinus and inferior regions of the skull. Delso *et al.*[74] proposed a similar approach for improved bone segmentation of UTE images using certain empirical rules to reduce the impact of misregistration errors, metal artifacts, and partial volume effects in MRI/CT training datasets. The methods described so far required a template or atlas registration to compensate the uncertainty of bone identification in UTE images. Roy *et al.*[34] proposed a patch-based method to obviate the need for atlas registration through matching the patches of voxels extracted from the target MR image to the reference dataset. Then, corresponding patches from the atlas database of CT images are combined via a Bayesian framework.

Juttukonda *et al.*[33] demonstrated a correlation between bone intensities in MR and CT images to assign patient-specific bone attenuation coefficients. The scatter plot derived from 97 subjects, where each point represents the intensity of bone tissue in UTE images versus CT number, suggested a strong sigmoid relationship ($R^2 = 0.95$). The proposed pseudo-CT generation required dual-echo UTE and two-point Dixon image acquisitions, where bony structures were extracted via thresholding of the R2 image generated from the UTE echo 1 and 2 images, which resulted in mean Dice coefficients of 0.75 ± 0.1 across 98 subjects for bone and 0.6 ± 0.1 for sinus air cavities.

2.B.3. Whole-body imaging

The variability and complexity of the human anatomy and the high level of noise and partial volume effect in MR sequences used for attenuation correction make the direct segmentation of bones from MR images a challenging task. Furthermore, application of UTE sequences for whole-body imaging is not yet customary owing to the long acquisition time and susceptibility to artifacts when using a large FOV. Therefore, the use of atlas registration for prediction of bone tissue is a common practice in whole-body MRI-guided attenuation generation.

Due to the large field-of-view, anatomical variability and moving organs atlas alignment errors are more pronounced in whole-body imaging. To alleviate this issue, Hofmann *et al.*[34] proposed a combination of atlas registration and pattern recognition method similar to the one described earlier for brain imaging[28] where a four-class MRI segmentation-based attenuation map (air, lung, water, and fat) was used to augment the robustness of GPR. Arabi and Zaidi[38] further improved the robustness of Hofmann's method to nonsystematic registration bias and anatomical abnormalities by exploiting a method to locally sort atlas images based on their similarity to the target image. In this way, the atlas images with locally gross misalignment errors would be discarded from training and pseudo-CT generation process. Yet, the high computational time required for elaborating and training the GPR is thought to be the major drawback of this method.

A time efficient scheme was proposed by Marshall *et al.*[37] which required only one online image registration to incorporate bone tissue in whole-body attenuation maps. A database of 121 CT images was created to match the target MRI via weighted heuristic measures to find the most similar CT in terms of body geometry before the atlas registration step. The similarity metrics consist of factors such as sex, weight, age, and fat to lean tissue ratio and lung volume. Then, the most similar CT in the atlas database was nonrigidly aligned to the target subject. MRI-based attenuation correction ignoring bone (standard four-class attenuation map) resulted in relative errors ranging from −37% to −8% in VOIs containing bone while the inclusion of bone reduced these errors from −3% to 4%. Paulus *et al.*[75] used a template of major body bones including left and right femur and hip, spine and skull to be registered to the target MR image separately. For the rest of the body, routine Dixon MRI-based segmentation AC was performed to generate a four-class attenuation map. This method is also time efficient since it requires just one template registration.

More recently, Arabi and Zaidi[66] implemented and compared a wide range of atlas-based attenuation map generation and bone segmentation methods of whole-body MR images. The accuracy of extracted bones was evaluated for different algorithms using PET/CT and MR Dixon images of 23 clinical studies. This included Hofmann's method,[34] arithmetic mean of whole aligned atlas dataset,[65] single template,[76] most similar atlas,[37] global,[77] and local weighting atlas fusion strategies.[30] Local weighting atlas fusion strategies based on standard image similarity measures such as the mean square distance and LNCC outperformed other methods. A representative slice of extracted whole-body bone along with error distance map obtained using the aforementioned methods is illustrated in Fig. 2.

Since existing MRI-based attenuation map generation approaches are not specifically designed for pediatric patients, Bezrukov *et al.*[78] assessed the impact of inter- and intrapatient variability of attenuation coefficients and anatomy. The quantitative accuracy of MRI-based attenuation correction based on an approach developed by the same authors[36] was evaluated using an adult and pediatric atlas on PET data of pediatric patients. The use of a dedicated atlas for pediatric patients resulted in improved attenuation map prediction and reduced interpatient bias variability.

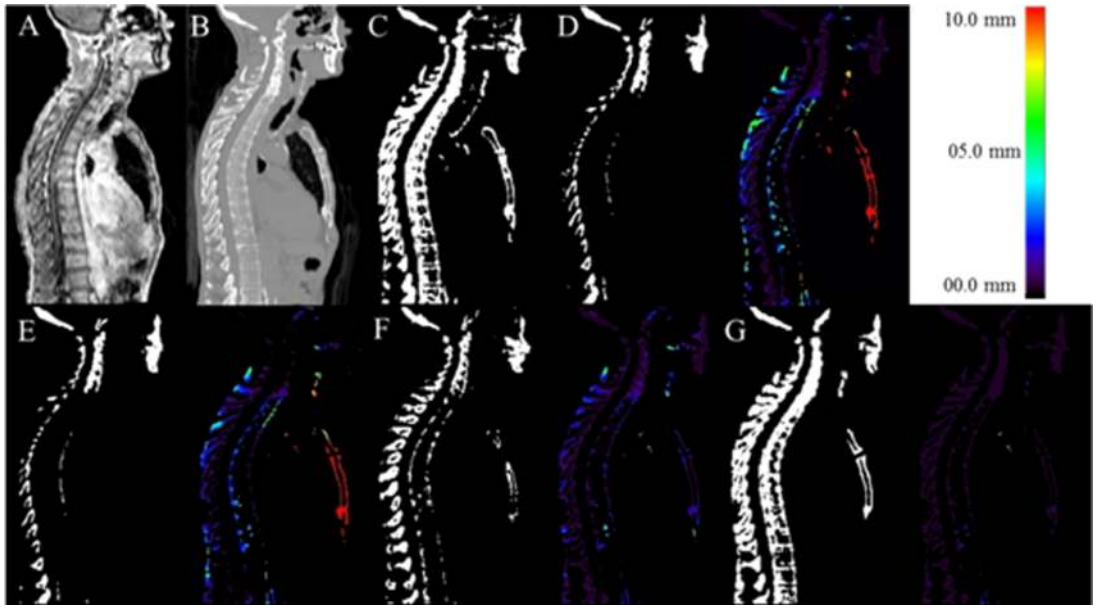

FIG. 2. Representative slice of bone segmentation from MR image along with corresponding error distance map. (A) In-phase MR image, (B) corresponding CT image, (C) binary image of reference bone, (D) Hofmann's method (Ref. 34), (E) arithmetic mean of whole aligned dataset, (F) global weighting atlas fusion, and (G) local weighting atlas fusion. Reprinted with permission from Arabi and Zaidi, "Comparison of atlas-based bone segmentation methods in whole-body PET/MRI," in *IEEE Nuclear Science Symposium and Medical Imaging Conference (NSS/MIC), Seattle, WA*, 2014. Copyright 2014 by © IEEE.

So far, atlas-based pseudo-CT generation methods exhibited superior performance compared to conventional segmentation-based methods in both whole-body and brain imaging. Multiatlas registration followed by local weighting atlas fusion resulted in promising pseudo-CT images and acceptable PET quantification. However, atlas-based methods may fail in cases with abnormal anatomy and in the presence of implants which are very unlikely to be present in atlas databases. Exploiting advanced segmentation and image processing techniques together with atlas-based methods can address this issue to provide more patient-specific attenuation maps. On the other hand, although the UTE MR sequence is able to extract bone signal, the high level of noise and presence of artifacts greatly influence its performance and application. Moreover, its long acquisition time limits its usage to only brain or small axial field-of-view (e.g., head and neck) imaging. However, the capability of the UTE sequence to provide patient-specific bone extraction makes it a valuable technique. Reducing its acquisition time and artifacts may render this approach the method of choice in the future, even in whole-body imaging studies.

2.C. Emission- and transmission-based methods

With advances in PET detector technology, TOF PET capability has been introduced in clinical PET/CT and PET/MRI systems, with the aim of improving image quality through the higher signal to noise ratio and enhanced lesion detectability. Following the resurfacing of TOF-PET, transmission- and emission-based methods have been revisited for deriving patient-specific attenuation maps in PET/MRI. In the following, we briefly review current state-of-the-art algorithms proposed so far for attenuation estimation.

2.C.1. Attenuation estimation using consistency conditions

Early attempts focused on the direct estimation of attenuation coefficients from emission data without using any estimate of the activity map based on the Helgason-Ludwig consistency conditions for emission data.[79] These conditions state that, in the absence of noise, a given emission data can only arise under certain attenuation conditions, or conversely for a given attenuation map; only certain emission data are possible. Based on the range of consistency conditions of the TOF attenuated Radon transform, Defrise *et al.*[39] recently showed that attenuation correction factors can be determined from TOF-PET data up to a constant scaling factor. They demonstrated that for all LORs containing activity, emission data determine the angular and radial derivatives of the Radon transform of the attenuation map. Rezaei *et al.*[80] extended this work to 3D TOF PET and only made use of the radial derivatives to estimate the attenuating volume. Li *et al.*[81] recently improved upon this approach by incorporating prior MR sinograms into the maximum *a posteriori* estimation of the attenuation sinogram from TOF emission data.

2.C.2. Attenuation estimation from only emission data

Emission-based estimation of attenuation coefficients was first proposed by Censor *et al.*[82] where an algebraic reconstruction technique was used to simultaneously reconstruct attenuation and activity maps. Nuyts *et al.*[83] further refined the concept of simultaneous maximum likelihood reconstruction of activity and attenuation (MLAA), in which the activity and attenuation were alternatively reconstructed using a

MLEM and a scaled gradient ascent algorithm. The MLAA algorithm had limited success owing to (i) inherent cross talk artifacts, i.e., the propagation of activity features into the attenuation map and vice versa, (ii) the limitations of activity support, i.e., the LORs that are out of the support of activity distribution (those without prompt coincidences) provide no information about the attenuation, and (iii) count statistics, which determine the level of noise in the estimated attenuation and activity maps. To reduce the cross talk and noise artifacts, Nuyts *et al.* imposed Gaussian tissue preference and Gibbs smoothness priors on the attenuation estimation.

With the advent of TOF PET/MRI scanners, Salomon *et al.*[41] imposed the inherent spatial constraint of TOF on activity estimation and MR anatomical information on attenuation map estimation within the MLAA algorithm. Thereby, the noise and cross talk artifacts were substantially reduced. As reported earlier by the same authors, the incorporated TOF information enables the reduction of cross talk artifacts.[84] Moreover, in their modified MLAA algorithm, the attenuation coefficients were estimated over many anatomical regions obtained from the segmentation of MRI. However, the segmentation of anatomical MR images is subject to errors, especially between bones and air in paranasal sinuses, or soft tissue close to the ribs and vertebrae.

Rezaei *et al.*[40] also demonstrated that TOF can suppress cross talk in the MLAA algorithm, consequently stabilizing the joint estimation problem. In addition, consistent with theoretical findings reported earlier,[39] they found that the reconstructed activity maps are globally scaled, while the attenuation maps show a position-dependent scaling. Later, Rezaei *et al.*[85] proposed a maximum likelihood algorithm that jointly estimates the activity distribution and the attenuation correction factors (MLACF). This method avoids the reconstruction of the attenuation map and is robust to errors in the detector pair sensitivities. Since MLACF does not estimate the attenuation map, the authors suggested using prior knowledge about the tracer distribution to correct for the scale problem. Bal *et al.*[86] studied the scale corrected MLACF algorithm using 57 FDG-PET/CT brain studies in comparison with the CTAC method serving as reference. They concluded that MLACF-based reconstruction can provide images that are both qualitatively and quantitatively equivalent to CT-based reconstructions.

Recently, Mehranian and Zaidi[87] proposed a MRI-guided MLAA algorithm for AC in whole-body PET/MR imaging. The algorithm imposes MRI spatial and CT statistical constraints on the estimation of attenuation maps using a constrained Gaussian mixture model (GMM) and Markov random field smoothness prior. Contrary to Salomon *et al.*,[41] they employed Dixon water and fat MR images, which were segmented into four known tissue classes, including outside air, lung, fat, and soft tissue and an unknown MR low-intensity class corresponding to air cavities, cortical bone, and susceptibility artifacts. The estimation of attenuation coefficients over the unknown/known classes was regularized using a mixture of Gaussians. It was demonstrated that the modified MLAA algorithm effectively suppresses noise, cross talk, and scaling problems of the joint estimation problem. In a companion clinical study,[42] the same authors showed that the four-class MRAC and their proposed MLAA-AC methods resulted in average SUV errors of −5.4% and −3.5% in lungs and −18.4% and −10.2% in bones, respectively. Despite the promise of MLAA-AC, a recent study pertaining to brain PET/MRI demonstrated that this approach has some limitations for this particular application and is actually outperformed by sophisticated atlas-based AC algorithms which provided the most accurate attenuation maps, and thus the lowest PET quantification bias.[88]

2.C.3. Attenuation estimation from emission and transmission data

Clinthorne *et al.*[89] reported the first study of joint maximum likelihood (ML) reconstruction of attenuation and activity images from emission and transmission data. However, these methods had a limited success as the transmission data are contaminated with emission data and vice versa.

Based on the capability of TOF technology in the separation of emission and transmission data,[90] Mollet *et al.*,[91] implemented a simultaneous transmission and emission acquisition on the Philips Ingenuity TF PET/MRI scanner[49] using an annulus-shaped transmission source. Despite the promising results, a companion study of five PET/MRI clinical datasets demonstrated that the limited TOF resolution of current PET scanners does not allow for perfect separation of transmission data from emission data,[43] which in turn results in nonuniformly scaled attenuation coefficients.

As demonstrated by Rezaei *et al.*,[40] the MLAA algorithm can estimate both activity and attenuation maps up to a scaling factor, which depends on the initial guess of the activity and attenuation maps. Furthermore, it was emphasized that the emission data do not provide information about the attenuation along the LORs located out-of-activity support. Panin *et al.*[44] proposed to make use of simultaneous emission and rotating rod sources transmission TOF data acquisition to stabilize the solution and solve the scaling and out-of-activity support problems. Similarly, Watson[92] proposed to use sparse line sources for transmission scanning in combination with emission data. It was concluded that the use of supplemental transmission data can significantly improve the accuracy of the estimated LACs in truncated regions as well as the quantitative performance of the emission-only MLAA algorithm. More recently, Rothfuss *et al.*[93] studied the feasibility of using the inherent background radiation of LSO crystals as transmission sources, where TOF information is employed to separate emission and LSO transmission data. The utilization of this additional information has pertinent implications when combined with emission data to stabilize and improve the MLAA algorithm.

2.C.4. Attenuation estimation from scattered coincidences

For the task of estimating activity and attenuation distributions from emission data of locally accumulating radiotracers, the projections that are out of the support

of the activity distribution (i.e., those without prompt coincidences but intersecting the patient's body) do not directly provide information about photon attenuation. However, these LORs might contain scattered coincidences that can provide additional information about attenuation they have experienced. Recently, Conti *et al.*[94] demonstrated that scattered coincidences can be used to reconstruct activity distributions using TOF and energy information. Sun and Pistorius[95] proposed a generalized scatter reconstruction algorithm to extract the activity distribution using both true and scattered coincidences by considering the limited energy resolution of PET detectors used in clinical practice. More recently, Berker *et al.*[96] proposed a scatter-to-attenuation backprojection to reconstruct PET attenuation coefficients from scattered-photon energies in the range of 248–478 keV. Their simulation results suggested that the attenuation map can be derived in the case of perfect spherical symmetry of attenuation and activity distributions as well as attenuation outside of the activity support.

3. CHALLENGES AND POTENTIAL SOLUTIONS

Section 2 focused on the various strategies followed to derive attenuation maps for PET attenuation correction using the information provided by MR images. However, a number of limitations and challenges, arising mostly from the inherent characteristics and constraints of MRI, have a significant impact on the accuracy of attenuation map derivation and PET quantification. Body truncation, metal and respiratory artifacts, MR coils attenuation, and patient-specific attenuation characteristics are among the most important challenging tasks. The technical aspects of these issues and the strategies developed to address them are discussed in Secs. 3.A–3.D.

3.A. MRI truncation compensation

The MRI transaxial FOV is limited owing to the deterioration of the homogeneity of the main magnetic field (B0) and linearity of gradient field, especially at the edge of the FOV. Therefore, the truncation of body organs at the edge of the FOV can occur in obese patients, which if not compensated for, can adversely affect MRAC of PET data.[97] Schramm *et al.*,[98] reported that arm truncation artifacts in 19 PET/MRI patient datasets led to an average SUV underestimation of less than 6% for VOIs defined in the trunk, while over the arms the errors were in the range of 16%–57%. Overall, three general approaches have been proposed to compensate for MRI FOV truncation including PET image segmentation, emission-based, and pure MRI-based approaches.

3.A.1. PET image segmentation

Hu *et al.*[16] proposed to compensate for truncation artifacts of three-class MRAC attenuation maps using the body contour delineated from uncorrected PET images. To better delineate the body contour, Delso *et al.*[97] proposed to segment PET images preliminary corrected for attenuation using truncated attenuation maps. Schramm *et al.*[98] followed a similar approach and employed a 3D contour identification using an automatically determined threshold. Using a TOF PET/MRI system, Qian *et al.*[99] demonstrated that the segmentation of NAC TOF PET images results in more accurate body contour delineation. However, thresholding-based separation of body contour and background air, even when using NAC TOF PET images, is sensitive to intensity variations and threshold selection. Blaffert *et al.*[100] compared threshold-based and gradient-based segmentation of body contour. They concluded that gradient-based segmentation results in better separation of the arms from the body and, thus leading to more accurate truncation compensation (Fig. 3). However, they found that the correction of truncated breasts is still challenging since in most NAC TOF PET images, air-breast tissue contrast is lower than air-to-arms tissue contrast.

3.A.2. Emission-based truncation compensation

Nuyts *et al.*[101] proposed to compensate the missing part of the MRI-derived attenuation map from non-TOF emission data using a constrained MLAA algorithm. The authors evaluated this method using five artificially truncated ^{18}F-FDG PET/CT studies and demonstrated that SUV underestimation errors were reduced from 20% to 7% for all voxels with SUVs

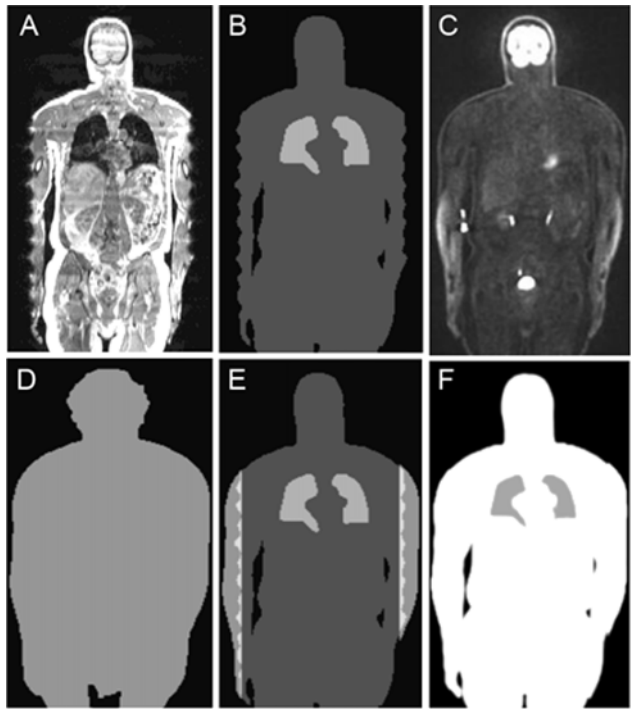

FIG. 3. PET/MRI truncation compensation using PET segmentation. (A) truncated T1-weighted MR image, (B) three-class MRAC map, (C) NAC TOF PET image, (D) body contour derived from segmentation of NAC TOF PET image, (E) overlap of the attenuation map and the identified truncation regions, and (F) final truncation compensated attenuation map. Adapted with permission from Blaffert *et al.*, "Comparison of threshold-based and watershed-based segmentation for the truncation compensation of PET/MR images," Proc. SPIE **8314**, 831403-1–831403-12 (2012). Copyright 2012 by SPIE.

larger than 1. In the MRI-guided MLAA algorithms described in Ref. 87, the authors suggested to segment the uncorrected or preliminary corrected PET images to identify the truncated regions in MR images. However, as mentioned earlier, the performance of the MLAA algorithm is dependent on the tracer biodistribution. For specific tracers with local uptake, emission-based techniques might have limited success.

3.A.3. Extended FOV MRI

The B0 inhomogeneities and gradient nonlinearities at the edges of the MRI transaxial FOV usually result in geometrically distorted or truncated body contours. To address these effects, Blumhagen *et al.*[102] proposed a method to extend the FOV using B0 homogenization with gradient enhancement (HUGE). The distortion artifacts outside the normal MRI FOV were noticeably reduced by this approach without any hardware modifications. The authors compared the performance of the HUGE algorithm with the MLAA algorithm using PET/MRI clinical studies.[103] Applying the HUGE method extended the FOV of the Dixon MRI from 50 to 60 cm, but at the expense of increased MRI data acquisition time. Overall, both truncation compensation methods improved the accuracy of derived attenuation maps with a trade-off of increased scanning time using the HUGE method and increased postprocessing time using the MLAA algorithm. The main advantage of HUGE over MLAA is that MRI-based FOV extension is independent of tracer distribution and kinetics.

3.B. MR susceptibility and respiratory artifact reduction

Void signal caused by metallic implants (blooming artifacts) can give rise to segmentation errors in segmentation-based MRAC methods as well as imperfect LAC prediction when using atlas-based learning techniques. It has been reported that the resulting erroneous attenuation map can lead to substantial SUV underestimation by about 50% in the case of hip prosthesis[36] and >100% in dental filling cases.[104] The correction of MR susceptibility artifacts has been explored using the following approaches.

3.B.1. Void regions segmentation

Ladefoged *et al.*[105] proposed to semiautomatically segment the signal voids caused by endoprotheses and to fill them with soft-tissue attenuation coefficients. It was demonstrated that the resulting attenuation maps can substantially reduce the underestimation of the SUVs. Schramm *et al.*[106] proposed an automatic approach to segment the body contour from preliminary attenuation-corrected PET images and T1-weighted MR image. The resulting body contour is filled by soft tissue, thereby isolated signal voids and particularly the artifacts connecting the background air to soft tissues and lungs are corrected. The lungs are then segmented using an intensity thresholding approach. Although simple filling of voids by soft-tissue attenuation coefficient is a first-line correction method, the authors reported a residual SUV bias of about −13% on average.

3.B.2. Atlas-based registration and emission-based estimation

Bezrukov *et al.*[36] proposed an atlas-based susceptibility artifact correction technique, in which the possible position of artifacts is identified using an atlas of artifact regions. The attenuation coefficients of the identified positions are estimated using an atlas-based registration method. Their results indicated that filling the voids with soft tissue reduces the quantification errors in lesions located within or near the artifacts from about −50% to −15%, while accounting for bones in the artifactual regions reduces the errors to <1%. Another approach for proper correction of artifacts that also accounts for the attenuation coefficients of metallic implants is the emission-based estimation of the attenuation coefficients using MLAA type of algorithms. Figure 4 shows the performance of the MLAA-GMM algorithm[87] in terms of estimating attenuation maps at 511 keV of a patient with unilateral hip prosthesis. As shown, the in-phase

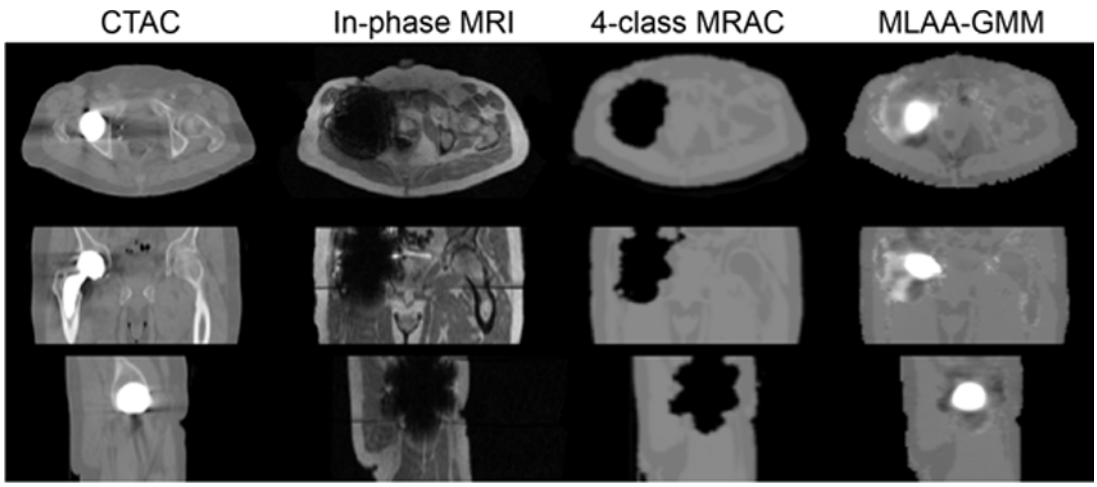

FIG. 4. The compensation of metal induced susceptibility artifacts in MRAC maps using the MRI-guided MLAA algorithm described in Ref. 87.

MR image and the resulting four-class MRAC attenuation map suffer substantially from the blooming artifacts. The MLAA algorithm, initialized with the four-class MRAC map, however, is capable of not only filling the void regions in an acceptable way but also estimating the attenuation coefficients of the metallic implant. Therefore, the results demonstrate that emission-based AC methods are promising for proper attenuation correction of PET images in the presence of extensive MR metallic artifacts.

3.B.3. Optimized MRI data acquisition

The dephasing of MR signal caused by metallic implants can be partially avoided using spin-echo and UTE sequences. In spin-echo sequences, 180° refocusing RF pulses are applied to reverse the dephasing induced by magnetic field inhomogeneity, while in UTE sequences, the MR signal is sampled immediately after RF excitation, so that the magnetization does not have enough time to be dephased.[17,107] Several techniques have also been developed for minimizing metal artifacts for fast spin-echo sequences, such as slice encoding for metal artifact correction (SEMAC) and multiacquisition with variable resonance image combination (MAVRIC).[17,108] Recently, Burger *et al.*[109,110] utilized diagnostic MAVRIC images to compensate for dental metal artifacts induced in Dixon-based attenuation maps. They demonstrated that accurate attenuation maps can be derived using this technique, yet at the expense of a considerably increased acquisition time.

Respiratory-phase mismatch between PET and MRI/CT attenuation maps is known to be another source of error in PET quantification. Owing to this mismatch, white-band banana artifacts usually occur around the heart and liver dome in PET images due to undercorrection for attenuation.[111] It has been shown that these artifacts result in errors of up to 24% in tracer uptake of liver tumors.[112] Methodologies for the correction of this type of artifacts can be classified into two categories which are briefly discussed below.

3.B.4. 4D attenuation map generation

Buerger *et al.*[112] explored the possibility of deriving 4D MRAC maps for AC of respiratory gated PET data. Respiratory synchronized MRI acquisitions were used to gate PET data acquisition and to derive motion vector fields. The gated data were then reconstructed using their corresponding phase-matched attenuation maps with respect to a reference respiratory phase. Since 4D MRI acquisition is time-consuming, Fayad *et al.*[113] proposed to derive motion fields from gated nonattenuation corrected PET images and to generate 4D MRI attenuation maps from end-expiration static MRI volumes. They demonstrated the potential of using 4D NAC PET images to derive 4D MRAC attenuation maps from a single static MRI volume.

3.B.5. Emission-based attenuation/motion estimation

Recently, Mehranian and Zaidi[114] investigated the potential of emission-based estimation of lung attenuation coefficients of four-class MRAC attenuation maps. They demonstrated that the proposed constrained MLAA algorithm can compensate for respiratory-phase mismatch as well as lung mis-segmentation errors, thus improving SUV quantification of liver and lung lesions. Rezaei and Nuyts[115] proposed a joint reconstruction and registration framework of gated PET data. In this framework, the gated PET activity and attenuation images are jointly reconstructed using the MLAA algorithm and registered to a reference frame using Demons registration algorithm. Using simulations, the authors demonstrated that this approach reduces the interframe registration error between activity and attenuation maps.

3.C. MR coils and other attenuating devices

Besides patient's body, several other objects such as RF coils, patient bed and patient positioning, and immobilization devices can contribute to photon attenuation and scattering in the FOV of PET/MRI systems. Ignoring surface RF coils in the attenuation map may lead to tracer underestimation of 19% (Ref. 116) and 15.5% (Ref. 117) in brain and whole-body PET imaging, respectively. Fürst *et al.*[118] reported that the patient's table results in 19% loss of true coincidences on the integrated Biograph mMR PET/MR system.

The attenuation of fixed objects, such as patient bed, body, and rigid coils (i.e., head/neck, spine, and torso) can be measured using transmission sources (^{68}Ge or ^{137}Cs)[119] or CT scans[120] and incorporated into attenuation maps as templates. The patient table and coil templates generated from transmission scans are more accurate than those generated from CT scans owing to the lack of streaking artifacts caused by high-density metallic components.[121] Moreover, the bilinear energy mapping of CT to attenuation coefficients at 511 keV for nonbiological materials might not be valid.[116] In this regard, Paulus *et al.*,[122] optimized the bilinear CT energy mapping procedure of hardware PET/MR components through the calibration of CT numbers of these components using transmission scanning and reported a reduction of SUV bias in the NEMA phantom from 3.1% to −0.5%.

The inclusion of flexible surface coils is more challenging because of their patient-specific application, positioning, and orientation. To determine the position of body matrix coil, Paulus *et al.*[123] applied two approaches: (i) cod liver oil capsules were attached to the surface of the coil as MR visible markers and (ii) UTE sequence was employed to image the coil. In the first approach, MR markers were rigidly registered to the same markers in the CT image of the coil using landmark-based registration. In the second approach, UTE images showed only parts of the coil's plastic housing and image registration to CT template was more difficult to achieve. Eldib *et al.*[124] studied several nonrigid registration algorithms to correctly deform CT templates to match MR coil markers. They found that the V-spline registration algorithm produced the most accurate registration compared to B-spline, thin-plate spline, and elastic body spline methods. Kartmann *et al.*[117] presented an approach for automatic localization of multiple RF surface coils in whole-body PET/MRI. In this approach, different marker patterns were used to distinguish

multiple partly overlapping RF surface coils. Nonrigid B-spline registration was used to register the corresponding markers on the CTAC template to the identified MR markers. The presented algorithm reliably reduced PET quantification errors due to overlooking the coils in the attenuation maps from 15.5% to 4.3%. Figure 5 shows the MR imaging setup of a subject with three overlapping RF surface coils together with coil CT templates overlaid on the four-class MARC map.[117]

Another approach for estimating the attenuation of MR invisible objects present in the FOV of PET/MRI scanners is to use emission- or transmission-based methods. In a simulation study, Nuyts *et al.*[101] demonstrated that the MLAA algorithm not only compensated for MR truncation artifacts but also retrieved six rods placed in the front of a torso phantom. In an experimental study, Rezaei *et al.*[40] showed that the MLAA algorithm can partially estimate the patient table. These approaches are promising; however, their robustness still needs to be characterized in different situations using large clinical databases.

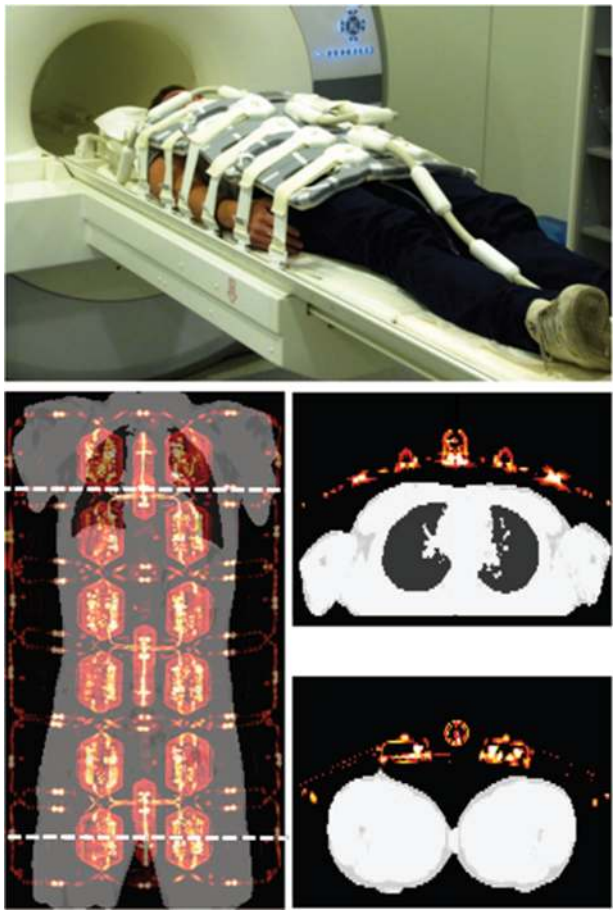

FIG. 5. Attenuation correction of flexible RF coils. Top: MR imaging setup of an exemplary volunteer with three overlapping RF surface coils. Bottom: combined four-class attenuation map of the volunteer with the registered CT-based attenuation maps of the overlapping RF coils. The dashed lines show the axial location of transverse slices. Adapted with permission from Kartmann *et al.*, "Integrated PET/MR imaging: Automatic attenuation correction of flexible RF coils," Med. Phys. **40**(8), 082301 (14pp.) (2013). Copyright 2013 by AAPM.

The standard coils currently employed on clinical MRI systems have not been designed to have low or zero photon attenuation but to provide the maximum signal-to-noise ratio in MR imaging. In PET/MR systems, these coils should be redesigned to have low photon attenuation without compromising their performance. Saha[125] redesigned the whole-body RF coil in a 3T simultaneous PET/MR system with minimal use of high density RF components in the PET FOV, thereby producing a zero PET attenuation whole-body coil. Dregely *et al.*[126] also developed a dedicated breast MR coil for the mMR scanner, in which PET attenuation was reduced by moving the high-density components, such as preamplifiers, away from the imaging FOV. However, to account for the overall photon attenuation and scattering in the coil, a CT-based template of the coil was acquired and coregistered to the coil's position for incorporation in four-class MRAC maps.

3.D. Inter/intrapatient variability of LACs

In segmentation-based Dixon and UTE MRAC methods, constant predefined attenuation coefficients are assigned to each tissue class. Therefore, intra- and interpatient variability of the attenuation coefficients is ignored, which can lead to non-negligible SUV errors especially in the lungs and bones. Atlas-based machine learning and emission-based AC methods are capable of providing more accurate estimates of patient-specific LACs of lungs and bones using the additional information available in atlas and emission data.

3.D.1. Lungs

Among the various tissue classes defined in segmentation-based MRAC methods, the lungs have the largest interpatient LAC variability with a standard deviation of 0.004 cm^{-1}.[18,48,127] In fact, the pulmonary parenchyma and vasculature vary considerably among patients by as much as 30%.[128] As such, different LACs have been assigned to lung tissue class, ranging from 0.018 to 0.035 cm^{-1}.[26,129] It has been reported that the assignment of a LAC of 0.024 cm^{-1} to the lungs produces relative errors of $13.5\% \pm 10.7\%$ (Ref. 34) and $7.7\% \pm 3.0\%$.[37] Conversely, the assignment of a LAC of 0.018 cm^{-1} to the lungs produces PET quantification bias of $1.9\% \pm 2.3\%$ (Ref. 26) and $-0.5 \pm 13.3\%$ (Ref. 56) in lung lesions and normal lung tissues. A small number of studies have focused on the derivation of patient-specific lung LACs considering lung tissue heterogeneity. The techniques reported so far can be classified into three categories: (i) prediction of mean lung LACs from MRI intensity and/or lung volume, (ii) atlas-based registration and learning, and (iii) emission-based estimation of lung LACs.

Marshall *et al.* established a linear mapping function between MRI and CT image intensities to predict the mean of lung LACs.[130] Lonn and Wollenweber[131] derived a linear relationship between lung volume and mean LACs. Both studies proved the improved performance of these approaches in terms of lung LAC prediction. However, as a general rule, the MRI-to-CT mapping function requires a standardized

MRI protocol and is influenced by the presence of respiratory motion, diamagnetic susceptibility, and flow-related artifacts, while the volume-to-LAC prediction model does not take into account the impact of other factors, such as gender, age, pathological conditions, and body positioning.

Atlas-based registration and machine learning techniques can, in principle, predict intrapatient variability of lung LACs. In the technique proposed by Hofmann *et al.*,[34] local structures of MR images and their corresponding CT atlases are incorporated into a GPR for prediction of LACs. In spite of promising results achieved for soft tissue and bony structures, this method exhibited large errors in the lungs owing to the insufficient signal produced by the lungs when using conventional MRI sequences. Recently, Arabi and Zaidi[38] embedded the correlation between lung volume and lung mean LACs into the GPR kernels and demonstrated that their improved method reduces the lung SUV bias from 8.9% (using Hofmann's approach) to 4.1%.

Emission-based derivation of lung LACs has also been explored by a few groups. Berker *et al.*[132] proposed a constrained TOF-MLAA algorithm for the estimation of mean lung LACs in five-class MRAC maps (including bone as the fifth class). The results obtained using Monte Carlo simulated PET/CT studies showed a high PET quantification bias, because of out-of-field accidental coincidences.

An alternative approach was investigated by Mehranian and Zaidi[114] using a MLAA algorithm constrained by a lung tissue preference prior for patient-specific lung LACs estimation of 19 PET/CT clinical studies. Their results showed that the standard four-class MRAC method resulted in an average SUV error of $-5.2\% \pm 7.1\%$ in the lungs, while the proposed MLAA algorithm reduced the error to $-0.8\% \pm 6.3\%$. Figure 6 compares the CTAC, MRAC, and MLAA attenuation maps of a patient whose lungs have a congested structure and high density gradients. As shown, the MLAA algorithm can accurately retrieve the lung density gradient in a continuous fashion, thus providing more accurate attenuation correction.

3.D.2. Bones

In segmentation-based methods, where bones are segmented as an additional tissue class using either UTE sequences or atlas-based approaches, the selection of appropriate bone tissue LAC is a subject of debate (see Table 2 in Ref. 7 for details) as different LACs have been used for the skull (range of 0.116–0.172 cm^{-1}) and whole-body cortical and spongious bones (range of 0.11–0.15 cm^{-1}). Schleyer *et al.*[133] demonstrated that the assignment of soft-tissue LAC to bones produces a lower SUV error than the assignment of cortical bone LACs, mainly because spongious bones have LACs of around 0.11 cm^{-1}.[18] In brain UTE imaging, Catana *et al.*,[11] evaluated the impact of eight different bone LACs ranging from 0.136 to 0.180 cm^{-1} on PET quantification. Their results suggested that the best bias-variability trade-off in PET quantification was achieved by assigning bone LACs of 0.143 and 0.151 cm^{-1}, as previously reported in Ref. 21.

Atlas-based AC methods can potentially estimate intrapatient variability of bone LACs by, for example, differentiating cortical bone in the skull from spongy bone in the vertebrae. Making use of the best atlas or local weighting of sorted atlases[30,36] can, in principle, capture the interpatient variability of the predicted bones.

Navalpakkam *et al.*[134] employed a UTE-based machine learning technique to predict continuous bone LACs. Their results showed that assigning a constant LAC value of 0.151 cm^{-1} to bone tissue class resulted in 4.2% SUV overestimation, while the continuously predicted bone LACs resulted in errors of 2.2%. Emission-based approaches are also

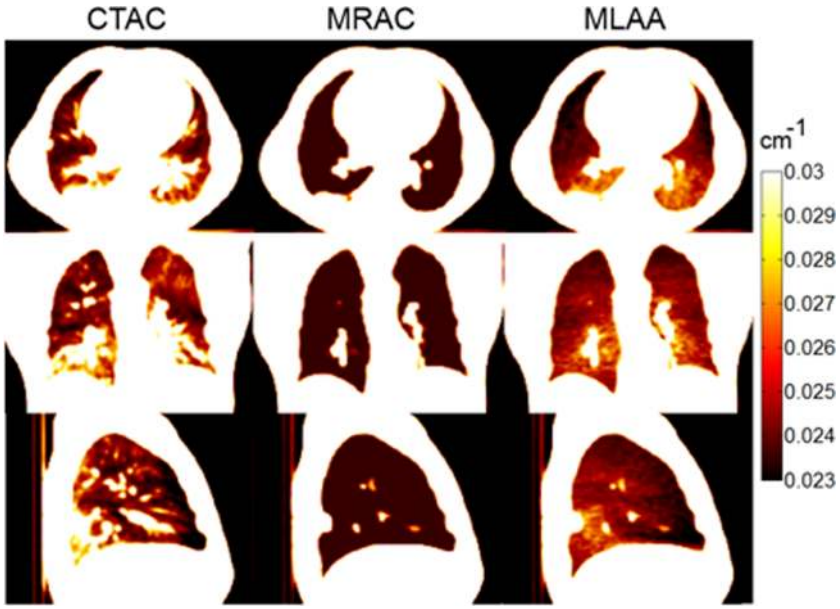

FIG. 6. Comparison of the attenuation maps of the standard four-class MRAC and the MRAC improved by the MLAA algorithm over the lungs with the reference CTAC maps in lung displaying windows. Adapted with permission from A. Mehranian and H. Zaidi, "Emission-based estimation of lung attenuation coefficients for attenuation correction in PET/MR," Phys. Med. Biol. **60**(12), 4813–4833 (2015). Copyright 2015 by IOP.

promising for estimation of patient-specific bone attenuation coefficients. A recent study reported a mean LAC for bone derived from CT images of five PET/CT/MRI datasets of 0.118 cm^{-1}, while the MLAA-GMM algorithm estimated a mean value of 0.104 cm^{-1}, which reduced the bias compared to the standard four-class MRAC method neglecting bone.[42]

3.D.3. MRI contrast agents

In contrast-enhanced MR imaging, the administration of small molecular weight paramagnetic contrast agents can have an impact on PET attenuation correction in PET/MRI. In experimental phantom studies, Lee *et al.*[135] evaluated the effects of MR contrast agents on PET quantification using different concentrations of gadolinium-based contrast agents on breast-cancer patients. Their results revealed that clinically relevant concentrations of MRI contrast media (<0.2 mmol) have negligible effects on the interpretation and quantification of PET images.

Lois *et al.*[136] also evaluated the effect of oral and intravenous MRI contrast media on PET quantification in PET/MRI. The results of CT and PET transmission measurements showed that clinically relevant concentrations of MRI contrast media have similar mean linear PET attenuation coefficients as water. Therefore, the administrated contrast agents did not result in noticeable quantification errors in the corresponding PET images. However, it was demonstrated that attenuation map mis-segmentation errors might occur after ingestion of superparamagnetic iron oxide (SPIO)-based contrast agents.

4. CURRENT TRENDS AND OPPORTUNITIES

4.A. Impact of time-of-flight on erroneous attenuation correction

During TOF PET image reconstruction, the image voxels are locally updated; therefore, error propagations are reduced in proportion to TOF timing resolution, while in non-TOF PET the propagated errors are proportional to the patient size.[137]

Wollenweber *et al.*[138] evaluated the effect of excluding an anterior array surface coil from the MRAC maps on PET quantification using TOF and non-TOF reconstructions. They found that with TOF information, the SUV errors due to neglecting the coil attenuation are slightly reduced from −8.2% to −7.3%. Davison *et al.*[139] evaluated the impact of TOF on reduction of PET quantification errors induced by metal artifact voids in MRAC maps of the TOF PET/MRI SIGNA system (GE Healthcare, Waukesha, WI) with nominal TOF time resolution of <400 ps.[140] It was found that the TOF capability significantly reduces the artifacts. The percentage error reduction with TOF ranged from 21% to 60% for medium-sized artifacts simulated in the maxilla and the sternum, respectively. Another study reported that TOF information improves image quality and diagnostic interpretation of PET images in the presence of attenuation artifacts.[141]

Mehranian and Zaidi[142] also studied the impact of TOF PET image reconstruction on the reduction of MRAC attenuation errors. Their results showed that non-TOF MRAC resulted in an average error of −3.4% and −21.8% in the lungs and bones, respectively, whereas the TOF reconstructions reduced the errors to −2.9% and −15.3%, respectively. Simulation studies also showed that as TOF time resolution improves, quantification errors are substantially reduced (Fig. 7). It was concluded that MRI-guided attenuation correction should be less of a concern on future TOF PET/MR scanners with improved timing resolution.

4.B. Advances in ultrashort and zero echo time MRI

Ultrashort echo time MRI sequences have been developed to depict tissues with low proton density and short T2 relaxation time, such as the lung and cortical bone. However, the acquisition of high-resolution UTE images is time-consuming, typically around 6 min in 3T brain imaging.[12] The acquisition time can be reduced by acquiring data with a coarser resolution, but this would lead to segmentation and learning errors for the task of attenuation correction. Recent attempts for accelerating UTE data acquisition focus on k-space undersampling in the context of CS and pMRI, or the combination of both.[143] Li *et al.*,[144] described a 3D

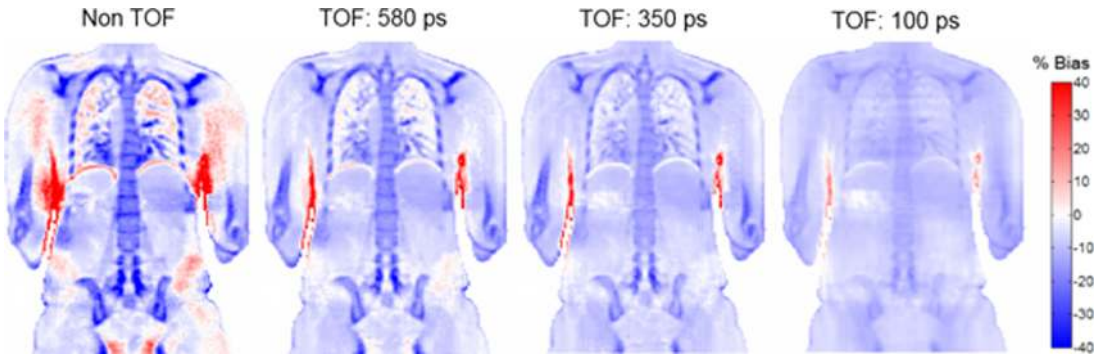

FIG. 7. Bias maps between PET image reconstructed by the four-class MRAC and CTAC maps without TOF and with different TOF resolutions in a whole-body phantom simulated from a clinical study. Adapted with permission from A. Mehranian and H. Zaidi, "Impact of time-of-flight PET on quantification errors in MRI-based attenuation correction," J. Nucl. Med. **56**(4), 635–641 (2015). Copyright 2015 by SNMMI.

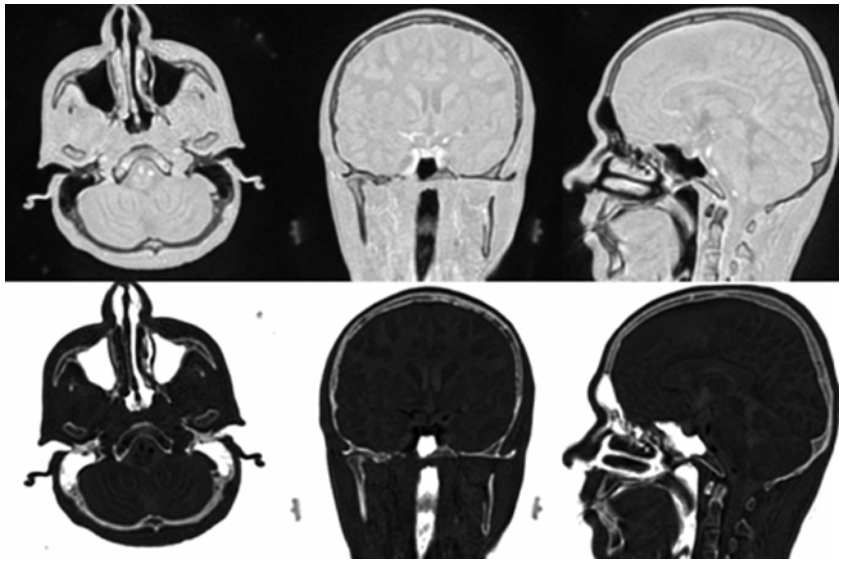

FIG. 8. High-resolution zero TE image of the head in linear (top) and inverse logarithmic (bottom) scale. Reprinted with permission from F. Wiesinger *et al.*, "Zero TE MR bone imaging in the head," Magn. Reson. Med. **75**, 107–114 (2015). Copyright 2015 by John Wiley and Sons.

CS UTE sequence with hybrid-radial encoding strategy and demonstrated the feasibility of their technique for achieving an acceleration factor of 10. Hu *et al.*[145] studied the acceleration of UTE scans through *k*-space sampling optimization. In this work, the angular sampling rate of 3D radial *k*-space trajectories was reduced from 100% to 25% for a series of UTE sequences with TEs in the range of 0.1–2.3 ms. The resulting scan times on the Philips 3T Achieva MRI system were in the range of 172 to 43 s. They demonstrated that high-quality bone-enhanced images can be generated using the UTE sequence with *k*-space undersampling as low as 25% (acceleration factor of 4) while preserving bone-air contrast at the cost of a minimal increase of noise level.

Aitken *et al.*[14] proposed to combine CS and sensitivity encoding[146] pMRI for accelerating dual-echo UTE by factors of 2–16. Their results showed that there is a good agreement between the fully sampled and undersampled maps with undersampling factors of up to 8 (scan time of 53 s). For higher acceleration, the contrast between bone and soft tissue was deteriorated leading to bone-air misclassification during the generation of MRAC maps. The sampling pattern in radial UTE sequences, however, does not meet sampling requirements of pMRI techniques, such as SENSE. Therefore, advanced non-Cartesian image reconstruction algorithms are required. Johansson *et al.*[15] studied two non-Cartesian parallel image reconstruction algorithms for the reconstruction of undersampled radial UTE and GRE data of 23 head datasets by factors of 3–30. The authors reported that for acceleration of up to a factor of 5, acceptable pseudo-CT images can be obtained by the reconstruction methods.

Promising advances were recently reported in the development of zero time echo (ZTE) sequences for imaging of short T2 structures in which signal readout starts instantaneously upon excitation leading to a nominal TE of zero.[147] Wiesinger *et al.*,[148] investigated a PD-weighted ZTE sequence for visualization and segmentation of the skull. In contrast to dual-echo UTE sequences, which mostly explore T2 time differences, the presented PD-weighted ZTE takes advantage of PD differences. Therefore, it eliminates the application of long T2 suppression methods. The authors studied standard and high-resolution protocols with acquisition times of about 3 and 6 min, respectively. Figure 8 shows a representative high-resolution ZTE and log-scaled images of the head.

Delso *et al.*[149] evaluated the feasibility of PD-weighted ZTE imaging for skull segmentation of 15 clinical studies acquired on a trimodality PET/CT-MR system. Quantitative evaluation based on the Jaccard distance between ZTE and corresponding CT bone masks showed improved performance of ZTE over dual-echo UTE by achieving overlap distances over the entire head of 38%–63% compared to 47%–79%. It was found that contrary to UTE, the presence of tendons on bone masks obtained with ZTE was minor. However, they reported remaining misclassifications at air/tissue interfaces, i.e., nasal cartilage and inner ear as in UTE.

Lung tissues are characterized by low PD and fast decaying signal. Recently, Johnson *et al.*[46] demonstrated the feasibility of free-breathing 3D radial UTE whole lung imaging. Radial undersampling and eight-channel pMRI were used to reduce scan time to 5.5 min. Gibiino *et al.*[150] studied a free-breathing 3D ZTE approach for visualization of lung parenchyma and vessels. They also demonstrated that high-quality images of lung parenchyma free from blurring and eddy-current artifacts can be obtained using ZTE in less than 6 min.

5. CONCLUDING REMARKS AND OUTLOOK

5.A. Technical aspects of MRI-guided attenuation correction in PET/MRI

The generation of accurate and patient-specific attenuation maps in whole-body PET/MRI is proving to be a challenging task. In this work, we critically reviewed the tremendous efforts carried out during the last decade

TABLE III. Comparison of pros and cons of the different categories of MRAC techniques used in PET/MRI.

	Segmentation-based	Atlas-based	Emission-based
Computation speed	+++	+	—
Simplicity and robustness	+++	+	+
Patient-specificity of lung LACs	—	+	++
Patient-specificity of bone LACs	—	++	++
Specific data requirement	—	+	+
MR truncation compensation	—	—	++
Coil attenuation estimation	—	—	+
MR susceptibility artifact reduction	—	+	++
Respiratory artifact reduction	—	—	+

for developing solutions and algorithms to address these challenges. We categorized the MRAC algorithms into three generic groups: segmentation, atlas registration, and learning and emission/transmission-based methods. The principles, algorithmic implementations, and recent advances in each category of methods were then elaborated. Each category of techniques has its own advantages and drawbacks from different standpoints and considering the various aspects.

Table III (inspired from Ref. 8) compares the general pros, cons, and potential of the three categories of techniques. Owing to their time-efficacy, simplicity, and robustness, segmentation-based MRAC is currently the method of choice implemented on virtually all current commercial PET/MRI scanners. In fact, robustness is one of the main prerequisites for the clinical adoption of an attenuation correction technique to guarantee accurate diagnosis and interpretation of PET findings. Since the introduction and wide adoption of segmentation-based MRAC methods on hybrid clinical PET/MRI systems (Philips Ingenuity and Siemens mMR PET/MRI scanners employ three-class[49] and four-class[151] MRAC, respectively), a number of studies have shown that their use on commercial PET/MRI systems provides images with similar or even improved diagnostic accuracy as PET/CT imaging.[152,153] However, these methods have some limitations and drawbacks, including reduced PET quantification accuracy in lesions located in/close to bones, lungs, and in regions presenting with artifacts. Czernin *et al.*[154] demonstrated comparable diagnostic performance of PET/MRI and PET/CT imaging based on clinical assessment of more than 900 patient studies. Since MRI is the modality of choice for providing the anatomical and functional information required by a number of oncological indications, PET/MRI would be a reasonable option provided the duration of imaging protocols and associated cost are kept to an acceptable level. New insights into disease phenotypes and biology can be provided by the complementary information imparted by hybrid PET/MR imaging. So far, it is becoming clear that PET/MRI presents diagnostic advantages in bone metastases and in prostate cancer, whereas it is outperformed by PET/CT in the assessment of lung nodules.[155]

On the other hand, atlas-based and emission-based methods are promising in terms of deriving more accurate attenuation maps, thus improving PET quantification. To provide an overall picture of the performance of these methods, Fig. 9 compares the attenuation maps of a representative clinical study produced using the segmentation-based four-class technique with atlas- and emission-based algorithms as

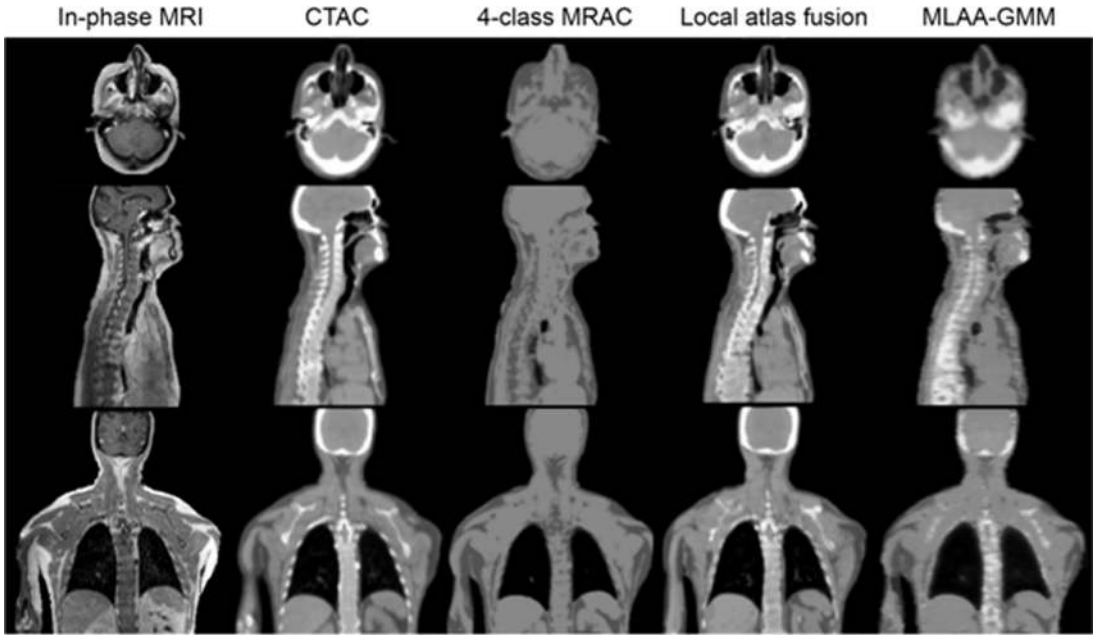

FIG. 9. Comparison of the attenuation maps obtained by the four-class segmentation-based method (Ref. 26), local weighted atlas fusion (Ref. 38), and a MRI-guided emission-based method (Ref. 87). Adapted with permission from Mehranian and Zaidi, "Clinical assessment of emission- and segmentation-based MRI-guided attenuation correction in whole body TOF PET/MRI," J. Nucl. Med. **56**(6), 877–883 (2015). Copyright 2015 by SNMMI.

compared to the CT-derived attenuation map serving as reference. As can be seen, atlas- and emission-based AC methods have successfully predicted/differentiated bones and air tissues compared to the standard four-class segmentation-based method. However, these two methods are still in their infancy and require extensive testing and in-depth clinical assessment to improve their robustness and efficacy. For instance, the performance of atlas registration-based methods depends on the collectivity of the MRI/CT training set and the efficiency of the learning algorithm. The performance of emission-based methods depends on TOF timing resolution and the PET tracer biodistribution. In brain imaging, several studies demonstrated that atlas-based segmentation or registration techniques can properly segment or predict bones.[30,70] Our ranking of patient-specificity of emission-based AC methods for lung and bone LACs is conservative as they are merely based on a few recent[42,116] studies showing the high potential of these methods for the derivation of lung LACs. However, further studies are required to demonstrate the performance of these AC methods for different tracers, cohorts of patients, and TOF resolutions. In fact, the performance of emission-based AC methods in deriving bones should be ranked conservatively based on current studies, since its performance is highly dependent on the TOF resolution, count level, and activity distribution. In addition, we conservatively ranked respiratory artifact reduction of emission-based AC methods. Indeed, evaluation and comparison with 4D attenuation correction are needed to demonstrate the potential of emission-based AC methods for this task.

In whole-body imaging, the combination of segmentation-based and atlas-based registration showed promising performance compared to that achieved by each method alone.[36] The combination of segmentation-based and lung emission-based attenuation correction has also been investigated showing a high potential of emission-based methods in deriving patient-specific lung LACs.[114] The results of comprehensive comparative evaluation studies can be exploited to come up with novel MRAC strategies taking advantage of the benefits of each technique.

MRI transaxial FOV truncation compensation through TOF NAC PET image segmentation or the MLAA algorithm is among the most promising approaches. Further investigation is still required to evaluate the efficiency and computational complexity of the two approaches. The attenuation coefficients of fixed and flexible objects (patient table, body coils, surface coils, etc.) are currently best accounted for using premeasured attenuation maps of fixed parts and deformable registration of templates for flexible parts.[117] Although emission-based algorithms can, in principle, estimate such attenuating objects, it remains to be demonstrated whether these techniques can accurately and completely estimate these objects given that they might have partial support of activity. As elaborated in this work, emission-based methods look promising for the correction of metal susceptibility artifacts by estimating the high attenuation coefficients of the metallic implants, which is not feasible using atlas-based registration techniques. On the MRI side, there have been some promising pulse sequence developments that can mitigate and reduce the extent of metal blooming artifacts. For the compensation of respiratory-phase mismatch between MRAC maps and PET images, two approaches are currently possible: (i) acquisition of 4D attenuation maps and (ii) simultaneous reconstruction of activity and attenuation. Emission-based methods are, however, as computationally intensive as atlas-based registration methods or even more. This further motivates the combination of these advanced methods with fast segmentation-based techniques. However, additional investigation is still required to further improve the accuracy and robustness of these attenuation correction methods to pave the way for their translation into clinical PET/MRI systems.

As an outlook, we believe that potential exciting developments to achieve accurate PET attenuation correction in PET/MRI, thus enabling improved PET quantification, can be broadly summarized in the following items: (i) The most promising attenuation correction methods will likely be achieved by hybrid techniques combining the three categories of MRAC methods to take advantage of the positive aspects of each class of methods. (ii) Technological advances in time-of-flight PET as well as U/ZTE MRI sequences will progressively continue to, respectively, provide opportunities in mitigating the adverse effects of inaccurate attenuation correction and deriving more accurate attenuation maps.

During the next decade, we shall witness further developments in PET detector technology and translation of digital silicon photomultipliers with new detector modules[156] from laboratory and preclinical settings into the clinical arena, assuring improved TOF capability and thus attenuation correction errors to an acceptable level. In addition, emission-based AC methods, which rely on information available in PET data to estimate attenuation maps, will show more promise as the TOF time resolution of PET scanners improves. With ongoing developments in instrumentation, we believe that a TOF PET time resolution of less than 100 ps might be possible in the future.[156,157] Thereby, one can anticipate improved robustness and availability of this type of attenuation correction methods in the near future, given their high potential compared to other techniques (Table III). With ongoing progress in parallel processing technology[158] and feasibility of real-time image reconstruction,[159] emission-based AC methods will also be certainly computationally appealing in clinical setting.

There have been remarkable advances in fast MRI data acquisition through parallel MRI and k-space undersampling to make the acquisition time of UTE MRI sequences clinically feasible. Moreover, the same trend was followed by the recent emergence of ZTE MRI sequence with promising characteristics for bone and lung parenchyma visualization in the context of PET/MRI. Certainly, these pulse sequences will continue to undergo further developments and improvements and will be made available in the clinic not only for attenuation correction but also for musculoskeletal and pulmonary disease evaluation.

5.B. Clinical perspectives of PET/MRI attenuation correction

The clinical impact of segmentation-based MRAC methods implemented on current generation PET/MRI scanners has been evaluated in a number of studies in terms of visible artifacts, lesion detectability, and quantification accuracy. Overall, there is a growing consensus that ignoring bones and tissue variability of attenuation coefficients in three- or four-class attenuation maps does not significantly impair lesion detectability and, in general, the diagnostic confidence of PET findings.[26,56] In addition, when PET molecular information is being complemented with MRI functional and morphological information, the number of equivocal findings can be substantially reduced, especially in soft-tissue neoplastic involvements typically encountered in prostate cancer,[160] head and neck cancers,[153,161–163] and gynecologic cancer.[164] However, the presence of artifacts in MRAC maps, particularly metal-susceptibility artifacts, can complicate the interpretation of PET findings[56] and even lead to false-positive or false-negative findings.[58] Therefore, similar to artifacts observed in PET/CT imaging, it has been strongly recommended to increase the diagnostic confidence by interpreting MRAC-PET images in conjunction with NAC-PET images. However , as highlighted in Secs. 4.A and 4.B, advances in TOF PET technology and Z/UTE MRI should enable to reduce or completely eradicate the frequency and the negative impact of these artifacts. Therefore, from a clinical perspective, the impact of artifacts and inaccuracies in attenuation maps is expected to be less of a concern, which might result in the adoption of new guidelines and procedures for PET interpretation.

The success of hybrid PET/MRI depends on the level of confidence revealed by current and future reports on clinical applications being explored where combined PET/MRI provides useful additional information. This might lead in the future to the widespread acceptance of PET/MRI in clinical setting, particularly in neurology and some applications in oncology.[165] However, the quantitative capability of PET imaging in PET/MRI with current AC methods has remained a major concern. Several reports from single-injection, dual-imaging studies demonstrated discrepancies in SUVs between PET/CT and PET/MR data, which were in many instances attributed to differences in the applied attenuation correction methods. The conclusions drawn from these studies should, however, be interpreted with some caution since time-dependent differences in tracer uptake owing to the nonstationary nature of FDG biodistribution were neglected. A number of studies used aligned CT and MR images to correct the same PET data, thus allowing a more straightforward assessment of the accuracy of MRAC in PET/MRI.

In most soft-tissue lesions, an average SUV bias of less than 10% has been found to be clinically irrelevant.[48] However, significant differences might be observed in some regions particularly the brain, spine, and lungs. Some investigators have suggested that ignoring bone could be acceptable in the abdominal and hip regions,[16,26,48] but probably not in the thorax.[52,166] There is a wide range of SUV underestimation for osseous lesions as reported by different groups. The bias was reported to be in the range of 5%–15% (Refs. 26 and 48) or up to 23% (Ref. 49) using PET/CT data, whereas simulation studies using an anthropomorphic thorax phantom reported a local bias of up to 17% (Ref. 18) or even 30%.[51] Overall, results reported so far seem to demonstrate that ignoring bone might not be adequate for quantification of osseous lesions.

The commonly accepted uncertainty in terms of dose calculation accuracy in radiation therapy planning is 5%. CT is commonly used as surrogate to estimate chemical composition. MRI is capable of probing soft-tissue properties with even greater accuracy and, as such, a combination of the information extracted from MRI and generated pseudo-CT images could give a better insight, particularly for particle radiation therapy where the beam range depends strongly on chemical composition.[69] In terms of dosimetric accuracy in radiation therapy treatment planning, the radiation dose distributions computed using generated pseudo-CT images agreed reasonably well with those derived using CT images (within 2%).[31,61,167,168]

Moving from the present to the future will involve tremendous evaluation and further development of the three main classes of attenuation correction strategies discussed in this work both in academic and corporate settings to achieve the best compromise. The assessment and comparison of the various attenuation correction techniques should continue in the context of multicentric clinical trials supported and implemented by manufacturers involving the use of large databases to assure the reproducibility and robustness of the developed algorithms. The outcomes of these trials will be vital for clinical adoption of the most promising approaches meeting the high-level standards required for their translation into clinical setting.

ACKNOWLEDGMENTS

This work was supported by the Swiss National Science Foundation under Grant No. SNSF 31003A-149957 and the Indo-Swiss Joint Research Programme No. ISJRP-138866.

[a]Author to whom correspondence should be addressed. Electronic mail: habib.zaidi@hcuge.ch; Telephone: +41 22 372 7258; Fax: +41 22 372 7169.

[1]H. Zaidi and A. D. Guerra, "An outlook on future design of hybrid PET/MRI systems," Med. Phys. **38**(10), 5667–5689 (2011).
[2]J. A. Disselhorst, I. Bezrukov, A. Kolb, C. Parl, and B. J. Pichler, "Principles of PET/MR imaging," J. Nucl. Med. **55**, 2S–10S (2014).
[3]S. Vandenberghe and P. K. Marsden, "PET-MRI: A review of challenges and solutions in the development of integrated multimodality imaging," Phys. Med. Biol. **60**(4), R115–R154 (2015).
[4]I. Bezrukov, F. Mantlik, H. Schmidt, B. Scholkopf, and B. J. Pichler, "MR-based PET attenuation correction for PET/MR imaging," Semin. Nucl. Med. **43**(1), 45–59 (2013).
[5]H. Zaidi, "Is MR-guided attenuation correction a viable option for dual-modality PET/MR imaging?," Radiology **244**(3), 639–642 (2007).
[6]M. Hofmann, B. Pichler, B. Schölkopf, and T. Beyer, "Towards quantitative PET/MRI: A review of MR-based attenuation correction techniques," Eur. J. Nucl. Med. Mol. Imaging **36**(1), 93–104 (2009).
[7]G. Wagenknecht, H. J. Kaiser, F. Mottaghy, and H. Herzog, "MRI for attenuation correction in PET: Methods and challenges," Magn. Reson. Mater. Phys., Biol. Med. **26**(1), 99–113 (2013).

[8]A. Martinez-Moller and S. G. Nekolla, "Attenuation correction for PET/MR: Problems, novel approaches and practical solutions," Z. Med. Phys. **22**(4), 299–310 (2012).
[9]V. Keereman, P. Mollet, Y. Berker, V. Schulz, and S. Vandenberghe, "Challenges and current methods for attenuation correction in PET/MR," Magn. Reson. Mater. Phys., Biol. Med. **26**(1), 81–98 (2013).
[10]H. Zaidi and B. H. Hasegawa, "Determination of the attenuation map in emission tomography," J. Nucl. Med. **44**(2), 291–315 (2003), see http://www.ncbi.nlm.nih.gov/pubmed/12571222.
[11]C. Catana, A. van der Kouwe, T. Benner, C. J. Michel, M. Hamm, M. Fenchel, B. Fischl, B. Rosen, M. Schmand, and A. G. Sorensen, "Toward implementing an MRI-based PET attenuation-correction method for neurologic studies on the MR-PET brain prototype," J. Nucl. Med. **51**(9), 1431–1438 (2010).
[12]V. Keereman, Y. Fierens, T. Broux, Y. De Deene, M. Lonneux, and S. Vandenberghe, "MRI-based attenuation correction for PET/MRI using ultrashort echo time sequences," J. Nucl. Med. **51**(5), 812–818 (2010).
[13]K. Zeimpekis, G. Delso, F. Wiesinger, P. Veit-Haibach, G. von Schulthess, and R. Grimm, "Investigation of 3D UTE MRI for lung PET attenuation correction [abstract]," J. Nucl. Med. **55**(Suppl. 1), 2103 (2014).
[14]A. Aitken, C. Kolbitsch, T. Schaeffter, C. Prieto Vasquez, A. Aitken, C. Kolbitsch, T. Schaeffter, and C. Prieto Vasquez, "Rapid acquisition of PET attenuation maps from highly undersampled UTE images using sparse-SENSE reconstruction," in *Proceedings of the 21st Annual Meeting of ISMRM, Salt Lake City, UT* (Lacke City, UT, 2013), p. 0769.
[15]A. Johansson, A. Garpebring, T. Asklund, and T. Nyholm, "CT substitutes derived from MR images reconstructed with parallel imaging," Med. Phys. **41**(8), 082302 (7pp.) (2014).
[16]Z. Hu, N. Ojha, S. Renisch, V. Schulz, I. Torres, D. Pal, G. Muswick, J. Penatzer, T. Guo, P. Boernert, C.-H. Tung, J. Kaste, L. Shao, M. Morich, T. Havens, P. Maniawski, W. Schaefer, R. Guenther, and G. Krombach, "MR-based attenuation correction for a whole-body sequential PET/MR system," in *IEEE Nuclear Science Symposium and Medical Imaging Conference (NSS/MIC)* (IEEE, Orlando, FL, 2009), pp. 3508–3512.
[17]B. A. Hargreaves, P. W. Worters, K. B. Pauly, J. M. Pauly, K. M. Koch, and G. E. Gold, "Metal-induced artifacts in MRI," Am. J. Roentgenol. **197**(3), 547–555 (2011).
[18]V. Keereman, R. V. Holen, P. Mollet, and S. Vandenberghe, "The effect of errors in segmented attenuation maps on PET quantification," Med. Phys. **38**(11), 6010–6019 (2011).
[19]F. L. Andersen, C. N. Ladefoged, T. Beyer, S. H. Keller, A. E. Hansen, L. Hojgaard, A. Kjaer, I. Law, and S. Holm, "Combined PET/MR imaging in neurology: MR-based attenuation correction implies a strong spatial bias when ignoring bone," NeuroImage **84**, 206–216 (2014).
[20]J. Teuho, J. Johansson, J. Linden, V. Saunavaara, T. Tolvanen, and M. Teras, "Specification and estimation of sources of bias affecting neurological studies in PET/MR with an anatomical brain phantom," Nucl. Instrum. Methods Phys. Res., Sect. A **734**, 179–184 (2014).
[21]H. Zaidi, M. L. Montandon, and D. O. Slosman, "Magnetic resonance imaging-guided attenuation and scatter corrections in three-dimensional brain positron emission tomography," Med. Phys. **30**(5), 937–948 (2003).
[22]G. Wagenknecht, E. R. Kops, L. Tellmann, and H. Herzog, "Knowledge-based segmentation of attenuation-relevant regions of the head in T1-weighted MR images for attenuation correction in MR/PET systems," in *IEEE Nuclear Science Symposium Conference Record (NSS/MIC)* (IEEE, Orlando, FL, 2009), pp. 3338–3343.
[23]G. Wagenknecht, E. R. Kops, J. Kaffanke, L. Tellmann, F. Mottaghy, M. D. Piroth, and H. Herzog, "CT-based evaluation of segmented head regions for attenuation correction in MR-PET systems," in *IEEE Nuclear Science Symposium and Medical Imaging Conference (NSS/MIC)* (IEEE, Knoxville, TN, 2010), pp. 2793–2797.
[24]E. Rota Kops, G. Wagenknecht, J. J. Scheins, L. Tellmann, and H. Herzog, "Attenuation correction in MR-PET scanners with segmented T1-weighted MR images," in *IEEE Nuclear Science Symposium and Medical Imaging Conference, Orlando, FL, 25-31 October 2009* (IEEE, Orlando, FL, 2009), pp. 2530–2533.
[25]Y. Berker, J. Franke, A. Salomon, M. Palmowski, H. C. Donker, Y. Temur, F. M. Mottaghy, C. Kuhl, D. Izquierdo-Garcia, Z. A. Fayad, F. Kiessling, and V. Schulz, "MRI-based attenuation correction for hybrid PET/MRI systems: A 4-class tissue segmentation technique using a combined ultrashort-echo-time/Dixon MRI sequence," J. Nucl. Med. **53**(5), 796–804 (2012).
[26]A. Martinez-Möller, M. Souvatzoglou, G. Delso, R. A. Bundschuh, C. Chefd'hotel, S. I. Ziegler, N. Navab, M. Schwaiger, and S. G. Nekolla, "Tissue classification as a potential approach for attenuation correction in whole-body PET/MRI: Evaluation with PET/CT data," J. Nucl. Med. **50**(4), 520–526 (2009).
[27]S. D. Wollenweber, S. Ambwani, A. R. Lonn, D. D. Shanbhag, S. Thiruvenkadam, S. Kaushik, R. Mullick, H. Qian, G. Delso, and F. Wiesinger, "Comparison of 4-class and continuous fat/water methods for whole-body, MR-based PET attenuation correction," IEEE Trans. Nucl. Sci. **60**(5), 3391–3398 (2013).
[28]M. Hofmann, F. Steinke, V. Scheel, G. Charpiat, J. Farquhar, P. Aschoff, M. Brady, B. Schölkopf, and B. J. Pichler, "MRI-based attenuation correction for PET/MRI: A novel approach combining pattern recognition and atlas registration," J. Nucl. Med. **49**(11), 1875–1883 (2008).
[29]S. L. S. Chan, Y. Gal, R. L. Jeffree, M. Fay, P. Thomas, S. Crozier, and Y. Zhengyi, "Automated classification of bone and air volumes for hybrid PET-MRI brain imaging," in *International Conference on Digital Image Computing: Techniques and Applications (DICTA), Hobart, Australia* (Springer, India, 2013), pp. 1–8.
[30]N. Burgos, M. Cardoso, K. Thielemans, M. Modat, J. Schott, J. Duncan, D. Atkinson, S. Arridge, B. Hutton, and S. Ourselin, "Attenuation correction synthesis for hybrid PET-MR scanners: Application to brain studies," IEEE Trans. Med. Imaging **33**(12), 2332–2341 (2014).
[31]D. Andreasen, K. Van Leemput, R. H. Hansen, J. A. Andersen, and J. M. Edmund, "Patch-based generation of a pseudo CT from conventional MRI sequences for MRI-only radiotherapy of the brain," Med. Phys. **42**(4), 1596–1605 (2015).
[32]A. Johansson, A. Garpebring, M. Karlsson, T. Asklund, and T. Nyholm, "Improved quality of computed tomography substitute derived from magnetic resonance (MR) data by incorporation of spatial information-potential application for MR-only radiotherapy and attenuation correction in positron emission tomography," Acta Oncol. **52**(7), 1369–1373 (2013).
[33]M. R. Juttukonda, B. G. Mersereau, Y. Chen, Y. Su, B. G. Rubin, T. L. Benzinger, D. S. Lalush, and H. An, "MR-based attenuation correction for PET/MRI neurological studies with continuous-valued attenuation coefficients for bone through a conversion from R2* to CT-Hounsfield units," NeuroImage **112**, 160–168 (2015).
[34]S. Roy, W.-T. Wang, A. Carass, J. L. Prince, J. A. Butman, and D. L. Pham, "PET attenuation correction using synthetic CT from ultrashort echo-time MR imaging," J. Nucl. Med. **55**(12), 2071–2077 (2014).
[35]M. Hofmann, I. Bezrukov, F. Mantlik, P. Aschoff, F. Steinke, T. Beyer, B. J. Pichler, and B. Scholkopf, "MRI-based attenuation correction for whole-body PET/MRI: Quantitative evaluation of segmentation- and atlas-based methods," J. Nucl. Med. **52**(9), 1392–1399 (2011).
[36]I. Bezrukov, H. Schmidt, F. Mantlik, N. Schwenzer, C. Brendle, B. Schölkopf, and B. J. Pichler, "MR-based attenuation correction methods for improved PET quantification in lesions within bone and susceptibility artifact regions," J. Nucl. Med. **54**(10), 1768–1774 (2013).
[37]H. R. Marshall, J. Patrick, D. Laidley, F. S. Prato, J. Butler, J. Théberge, R. T. Thompson, and R. Z. Stodilka, "Description and assessment of a registration-based approach to include bones for attenuation correction of whole-body PET/MRI," Med. Phys. **40**(8), 082509 (10pp.) (2013).
[38]H. Arabi and H. Zaidi, "MRI-based pseudo-CT generation using sorted atlas images in whole-body," *IEEE Nuclear Science Symposium and Medical Imaging Conference (NSS/MIC), Seattle, WA, 2014*.
[39]M. Defrise, A. Rezaei, and J. Nuyts, "Time-of-flight PET data determine the attenuation sinogram up to a constant," Phys. Med. Biol. **57**(4), 885–899 (2012).
[40]A. Rezaei, M. Defrise, G. Bal, C. Michel, M. Conti, C. Watson, and J. Nuyts, "Simultaneous reconstruction of activity and attenuation in time-of-flight PET," IEEE Trans. Med. Imaging **31**(12), 2224–2233 (2012).
[41]A. Salomon, A. Goedicke, B. Schweizer, T. Aach, and V. Schulz, "Simultaneous reconstruction of activity and attenuation for PET/MR," IEEE Trans. Med. Imaging **30**(3), 804–813 (2011).
[42]A. Mehranian and H. Zaidi, "Clinical assessment of emission- and segmentation-based MRI-guided attenuation correction in whole body TOF PET/MRI," J. Nucl. Med. **56**(6), 877–883 (2015).
[43]P. Mollet, V. Keereman, J. Bini, D. Izquierdo-Garcia, Z. A. Fayad, and S. Vandenberghe, "Improvement of attenuation correction in time-of-flight PET/MR imaging with a positron-emitting source," J. Nucl. Med. **55**(2), 329–336 (2014).
[44]V. Y. Panin, M. Aykac, and M. E. Casey, "Simultaneous reconstruction of emission activity and attenuation coefficient distribution from TOF data, acquired with external transmission source," Phys. Med. Biol. **58**(11), 3649–3669 (2013).

[45]G. Delso, M. Carl, F. Wiesinger, L. Sacolick, M. Porto, M. Hüllner, A. Boss, and P. Veit-Haibach, "Anatomic evaluation of 3-dimensional ultrashort-echo-time bone maps for PET/MR attenuation correction," J. Nucl. Med. **55**(5), 780–785 (2014).
[46]K. M. Johnson, S. B. Fain, M. L. Schiebler, and S. Nagle, "Optimized 3D ultrashort echo time pulmonary MRI," Magn. Reson. Med. **70**(5), 1241–1250 (2013).
[47]Z. Hu, S. Renisch, B. Schweizer, T. Blaffert, N. Ojha, T. Guo, J. Tang, C. Tung, J. Kaste, V. Schulz, I. Torres, and L. Shao, "MR-based attenuation correction for whole-body PET/MR system," in *IEEE Nuclear Science Symposium and Medical Imaging Conference (NSS/MIC)* (IEEE, Knoxville, TN, 2010), pp. 2119–2122.
[48]V. Schulz, I. Torres-Espallardo, S. Renisch, Z. Hu, N. Ojha, P. Börnert, M. Perkuhn, T. Niendorf, W. M. Schäfer, H. Brockmann, T. Krohn, A. Buhl, R. W. Günther, F. M. Mottaghy, and G. A. Krombach, "Automatic, three-segment, MR-based attenuation correction for whole-body PET/MR data," Eur. J. Nucl. Med. Mol. Imaging **38**(1), 138–152 (2011).
[49]H. Zaidi, N. Ojha, M. Morich, J. Griesmer, Z. Hu, P. Maniawski, O. Ratib, D. Izquierdo-Garcia, Z. A. Fayad, and L. Shao, "Design and performance evaluation of a whole-body ingenuity TF PET-MRI system," Phys. Med. Biol. **56**(10), 3091–3106 (2011).
[50]M. Eiber, A. Martinez-Möller, M. Souvatzoglou, K. Holzapfel, A. Pickhard, D. Löffelbein, I. Santi, E. Rummeny, S. Ziegler, M. Schwaiger, S. Nekolla, and A. Beer, "Value of a Dixon-based MR/PET attenuation correction sequence for the localization and evaluation of PET-positive lesions," Eur. J. Nucl. Med. Mol. Imaging **38**(9), 1691–1701 (2011).
[51]A. Samarin, C. Burger, S. Wollenweber, D. Crook, I. Burger, D. Schmid, G. von Schulthess, and F. Kuhn, "PET/MR imaging of bone lesions—Implications for PET quantification from imperfect attenuation correction," Eur. J. Nucl. Med. Mol. Imaging **39**(7), 1154–1160 (2012).
[52]M. C. Aznar, R. Sersar, J. Saabye, C. N. Ladefoged, F. L. Andersen, J. H. Rasmussen, J. Lofgren, and T. Beyer, "Whole-body PET/MRI: The effect of bone attenuation during MR-based attenuation correction in oncology imaging," Eur. J. Radiol. **83**(7), 1177–1183 (2014).
[53]J. Ouyang, C. Se Young, Y. Petibon, A. A. Bonab, N. Alpert, and G. El Fakhri, "Bias atlases for segmentation-based PET attenuation correction using PET-CT and MR," IEEE Trans. Nucl. Sci. **60**(5), 3373–3382 (2013).
[54]A. Akbarzadeh, M. R. Ay, A. Ahmadian, N. Riahi Alam, and H. Zaidi, "MRI-guided attenuation correction in whole-body PET/MR: Assessment of the effect of bone attenuation," Ann. Nucl. Med. **27**(2), 152–162 (2013).
[55]S. Keller, S. Holm, A. Hansen, B. Sattler, F. Andersen, T. Klausen, L. Højgaard, A. Kjær, and T. Beyer, "Image artifacts from MR-based attenuation correction in clinical, whole-body PET/MRI," Magn. Reson. Mater. Phys., Biol. Med. **26**(1), 173–181 (2013).
[56]H. Arabi, O. Rager, A. Alem, A. Varoquaux, M. Becker, and H. Zaidi, "Clinical assessment of MR-guided 3-class and 4-class attenuation correction in PET/MR," Mol. Imaging Biol. **17**(2), 264–276 (2015).
[57]H. Choi, G. J. Cheon, H. J. Kim, S. H. Choi, J. S. Lee, Y. I. Kim, K. W. Kang, J. K. Chung, E. E. Kim, and D. S. Lee, "Segmentation-based MR attenuation correction including bones also affects quantitation in brain studies: An initial result of ^{18}F-FP-CIT PET/MR for patients with parkinsonism," J. Nucl. Med. **55**(10), 1617–1622 (2014).
[58]C. Brendle, H. Schmidt, A. Oergel, I. Bezrukov, M. Mueller, C. Schraml, C. Pfannenberg, C. la Fougere, K. Nikolaou, and N. Schwenzer, "Segmentation-based attenuation correction in positron emission tomography/magnetic resonance: Erroneous tissue identification and its impact on positron emission tomography interpretation," Invest. Radiol. **50**(5), 339–346 (2015).
[59]C. N. Ladefoged, A. E. Hansen, S. H. Keller, B. M. Fischer, J. H. Rasmussen, I. Law, A. Kjær, L. Højgaard, F. Lauze, and T. Beyer, "Dental artifacts in the head and neck region: Implications for Dixon-based attenuation correction in PET/MR," EJNMMI Phys. **2**(1), 8–22 (2015).
[60]Y. C. Tai, K. P. Lin, M. Dahlbom, and E. J. Hoffman, "A hybrid attenuation correction technique to compensate for lung density in 3-D total body PET," IEEE Trans. Nucl. Sci. **43**(1), 323–330 (1996).
[61]T. Chang, R. H. Diab, J. W. Clark, and O. R. Mawlawi, "Investigating the use of nonattenuation corrected PET images for the attenuation correction of PET data," Med. Phys. **40**(8), 082508 (11pp.) (2013).
[62]M.-L. Montandon and H. Zaidi, "Atlas-guided non-uniform attenuation correction in cerebral 3D PET imaging," NeuroImage **25**(1), 278–286 (2005).
[63]H. Zaidi, M.-L. Montandon, and S. Meikle, "Strategies for attenuation compensation in neurological PET studies," NeuroImage **34**(2), 518–541 (2007).
[64]S. D. Wollenweber, S. Ambwani, G. Delso, A. H. R. Lonn, R. Mullick, F. Wiesinger, Z. Piti, A. Tari, G. Novak, and M. Fidrich, "Evaluation of an atlas-based PET head attenuation correction using PET/CT & MR patient data," IEEE Trans. Nucl. Sci. **60**(5), 3383–3390 (2013).
[65]J. Uh, T. E. Merchant, Y. Li, X. Li, and C. Hua, "MRI-based treatment planning with pseudo CT generated through atlas registration," Med. Phys. **41**(5), 051711 (8pp.) (2014).
[66]H. Arabi and H. Zaidi, "Comparison of atlas-based bone segmentation methods in whole-body PET/MRI," in *IEEE Nuclear Science Symposium and Medical Imaging Conference (NSS/MIC), Seattle, WA*, 2014.
[67]D. Izquierdo-Garcia, A. E. Hansen, S. Forster, D. Benoit, S. Schachoff, S. Furst, K. T. Chen, D. B. Chonde, and C. Catana, "An SPM8-based approach for attenuation correction combining segmentation and nonrigid template formation: Application to simultaneous PET/MR brain imaging," J. Nucl. Med. **55**(11), 1825–1830 (2014).
[68]Z. Yang, J. Choupan, F. Sepehrband, D. Reutens, and S. Crozier, "Tissue classification for PET/MRI attenuation correction using conditional random field and image fusion," Int. J. Mach. Learn. Comput. **3**(1), 87–98 (2013).
[69]J. Sjölund, D. Forsberg, M. Andersson, and H. Knutsson, "Generating patient specific pseudo-CT of the head from MR using atlas-based regression," Phys. Med. Biol. **60**(2), 825–839 (2015).
[70]A. Johansson, M. Karlsson, J. Yu, T. Asklund, and T. Nyholm, "Voxel-wise uncertainty in CT substitute derived from MRI," Med. Phys. **39**(6), 3283–3290 (2012).
[71]N. Burgos, M. J. Cardoso, M. Modat, S. Pedemonte, J. Dickson, A. Barnes, J. S. Duncan, D. Atkinson, S. R. Arridge, and B. F. Hutton, "Attenuation correction synthesis for hybrid PET-MR scanners," in *Medical Image Computing and Computer-Assisted Intervention–MICCAI* (Springer, Berlin Heidelberg, 2013), pp. 147–154.
[72]A. S. Ribeiro, E. R. Kops, H. Herzog, and P. Almeida, "Hybrid approach for attenuation correction in PET/MR scanners," Nucl. Instrum. Methods Phys. Res., Sect. A **734**, 166–170 (2014).
[73]C. B. Poynton, K. T. Chen, D. B. Chonde, D. Izquierdo-Garcia, R. L. Gollub, E. R. Gerstner, T. T. Batchelor, and C. Catana, "Probabilistic atlas-based segmentation of combined T1-weighted and DUTE MRI for calculation of head attenuation maps in integrated PET/MRI scanners," Am. J. Nucl. Med. Mol. Imaging **4**(2), 160–171 (2014).
[74]G. Delso, K. Zeimpekis, M. Carl, F. Wiesinger, M. Hüllner, and P. Veit-Haibach, "Cluster-based segmentation of dual-echo ultra-short echo time images for PET/MR bone localization," EJNMMI Phys. **1**(1), 1–13 (2014).
[75]D. H. Paulus, H. H. Quick, C. Geppert, M. Fenchel, Y. Zhan, G. Hermosillo, D. Faul, F. Boada, K. P. Friedman, and T. Koesters, "Whole-body PET/MR imaging: Quantitative evaluation of a novel model-based MR attenuation correction method including bone," J. Nucl. Med. **56**(7), 1061–1066 (2015).
[76]E. Rota Kops and H. Herzog, "Template based attenuation correction for PET in MR-PET scanners," in *IEEE Nuclear Science Symposium Conference Record* (IEEE, Dresden, Germany, 2008), pp. 3786–3789.
[77]Y. Xia, J. Fripp, S. S. Chandra, R. Schwarz, C. Engstrom, and S. Crozier, "Automated bone segmentation from large field of view 3D MR images of the hip joint," Phys. Med. Biol. **58**(20), 7375–7390 (2013).
[78]I. Bezrukov, H. Schmidt, S. Gatidis, F. Mantlik, J. F. Schäfer, N. F. Schwenzer, and B. J. Pichler, "Quantitative evaluation of segmentation-and atlas-based attenuation correction for PET/MR on pediatric patients," J. Nucl. Med. **56**(7), 1067–1074 (2015).
[79]F. Natterer, "Determination of tissue attenuation in emission tomography of optically dense media," Inverse Probl. **9**(6), 731–736 (1993).
[80]A. Rezaei, J. Nuyts, and M. Defrise, "Analytic reconstruction of the attenuation from 3D time-of-flight PET data," in *IEEE Nuclear Science Symposium and Medical Imaging Conference (NSS/MIC)* (IEEE, Anaheim, CA, 2012), pp. 2330–2333.
[81]H. Li, G. El Fakhri, and Q. Li, "Direct MAP estimation of attenuation sinogram using TOF PET data and anatomical information," in *Proceedings of Fully 3D Image Reconstruction in Radiology and Nuclear Medicine* (Orlando, FL, 2013), pp. 404–407.
[82]Y. Censor, D. E. Gustafson, A. Lent, and H. Tuy, "A new approach to the emission computerized tomography problem: Simultaneous calculation of attenuation and activity coefficients," IEEE Trans. Nucl. Sci. **26**(2), 2775–2779 (1979).

[83]J. Nuyts, P. Dupont, S. Stroobants, R. Benninck, L. Mortelmans, and P. Suetens, "Simultaneous maximum a posteriori reconstruction of attenuation and activity distributions from emission sinograms," IEEE Trans. Med. Imaging **18**(5), 393–403 (1999).
[84]A. Salomon, A. Goedicke, and T. Aach, "Simultaneous reconstruction of activity and attenuation in multi-modal ToF-PET," in *International Meeting on Fully Three-Dimensional Image Reconstruction in Radiology and Nuclear Medicine (Fully3D), Beijing, China, 5-10 September 2009* (Beijing, China, 2009), pp. 339–342.
[85]A. Rezaei, M. Defrise, and J. Nuyts, "ML-reconstruction for TOF-PET with simultaneous estimation of the attenuation factors," IEEE Trans. Med. Imaging **33**(7), 1563–1572 (2014).
[86]G. Bal, F. Kehren, C. Michel, C. Watson, D. Manthey, and J. Nuyts, "Clinical evaluation of MLAA for MR-PET [abstract]," J. Nucl. Med. **52**(Suppl. 1), 263 (2011).
[87]A. Mehranian and H. Zaidi, "Joint estimation of activity and attenuation in whole-body TOF PET/MRI using constrained Gaussian mixture models," IEEE Trans. Med. Imaging **34**(9), 1808–1821 (2015).
[88]A. Mehranian, H. Arabi, and H. Zaidi, "Quantitative analysis of MRI-guided attenuation correction methods in time-of-flight brain PET/MRI," NeuroImage (in press).
[89]N. H. Clinthorne, J. A. Fessler, G. D. Hutchins, and W. L. Rogers, "Joint maximum likelihood estimation of emission and attenuation densities in PET," in *Conference Record of the IEEE Nuclear Science Symposium and Medical Imaging Conference* (IEEE, Santa Fe, NM, 1991), pp. 1927–1932.
[90]W. W. Moses, "Time of flight in PET revisited," IEEE Trans. Nucl. Sci. **50**(5), 1325–1330 (2003).
[91]P. Mollet, V. Keereman, E. Clementel, and S. Vandenberghe, "Simultaneous MR-compatible emission and transmission imaging for PET using time-of-flight information," IEEE Trans. Med. Imaging **31**, 1734–1742 (2012).
[92]C. C. Watson, "Supplemental transmission method for improved PET attenuation correction on an integrated MR/PET," Nucl. Instrum. Methods Phys. Res., Sect. A **734**(Part B), 191–195 (2014).
[93]H. Rothfuss, V. Panin, A. Moor, J. Young, I. Hong, C. Michel, J. Hamill, and M. Casey, "LSO background radiation as a transmission source using time of flight," Phys. Med. Biol. **59**(18), 5483–5500 (2014).
[94]M. Conti, I. Hong, and C. Michel, "Reconstruction of scattered and unscattered PET coincidences using TOF and energy information," Phys. Med. Biol. **57**(15), N307–N317 (2012).
[95]H. Sun and S. Pistorius, "A generalized scatter reconstruction algorithm for limited energy resolution PET detectors," *IEEE Nuclear Science Symposium and Medical Imaging Conference (NSS/MIC), Seattle, WA, 2014*.
[96]Y. Berker, F. Kiessling, and V. Schulz, "Scattered PET data for attenuation-map reconstruction in PET/MRI," Med. Phys. **41**(10), 102502 (13pp.) (2014).
[97]G. Delso, A. Martinez-Möller, R. A. Bundschuh, S. G. Nekolla, and S. I. Ziegler, "The effect of limited MR field of view in MR/PET attenuation correction," Med. Phys. **37**(6), 2804–2812 (2010).
[98]G. Schramm, J. Langner, F. Hofheinz, J. Petr, A. Lougovski, B. Beuthien-Baumann, I. Platzek, and J. van den Hoff, "Influence and compensation of truncation artifacts in MR-based attenuation correction in PET/MR," IEEE Trans. Med. Imaging **32**(11), 2056–2063 (2013).
[99]H. Qian, R. M. Manjeshwar, S. Ambwani, and S. D. Wollenweber, "Truncation completion of MR-based PET attenuation maps using time-of-flight non-attenuation-corrected PET images," in *IEEE Nuclear Science Symposium and Medical Imaging Conference (NSS/MIC)* (IEEE, Anaheim, CA, 2012), pp. 2773–2775.
[100]T. Blaffert, S. Renisch, J. Tang, M. Narayanan, and Z. Hu, "Comparison of threshold-based and watershed-based segmentation for the truncation compensation of PET/MR images," Proc. SPIE **8314**, 831403-1–831403-12 (2012).
[101]J. Nuyts, G. Bal, F. Kehren, M. Fenchel, C. Michel, and C. Watson, "Completion of a truncated attenuation image from the attenuated PET emission data," IEEE Trans. Med. Imaging **32**(2), 237–246 (2013).
[102]J. O. Blumhagen, R. Ladebeck, M. Fenchel, and K. Scheffler, "MR-based field-of-view extension in MR/PET: B_0 homogenization using gradient enhancement (HUGE)," Magn. Reson. Med. **70**(4), 1047–1057 (2013).
[103]J. O. Blumhagen, H. Braun, R. Ladebeck, M. Fenchel, D. Faul, K. Scheffler, and H. H. Quick, "Field of view extension and truncation correction for MR-based human attenuation correction in simultaneous MR/PET imaging," Med. Phys. **41**(2), 022303 (9pp.) (2014).
[104]C. N. Ladefoged, T. Beyer, S. H. Keller, I. Law, L. Hojgaard, A. Kjær, F. Lauze, and F. L. Andersen, "PET/MR imaging of head/neck in the presence of dental implants: Reducing image artifacts and increasing accuracy through inpainting [abstract]," Annual Congress of the European Association of Nuclear Medicine, 601 (2013).
[105]C. Ladefoged, F. Andersen, S. Keller, J. Löfgren, A. Hansen, S. Holm, L. Højgaard, and T. Beyer, "PET/MR imaging of the pelvis in the presence of endoprostheses: Reducing image artifacts and increasing accuracy through inpainting," Eur. J. Nucl. Med. Mol. Imaging **40**(4), 594–601 (2013).
[106]G. Schramm, J. Maus, F. Hofheinz, J. Petr, A. Lougovski, B. Beuthien-Baumann, I. Platzek, and J. van den Hoff, "Evaluation and automatic correction of metal-implant-induced artifacts in MR-based attenuation correction in whole-body PET/MR imaging," Phys. Med. Biol. **59**(11), 2713–2726 (2014).
[107]M. J. Lee, S. Kim, S. A. Lee, H. T. Song, Y. M. Huh, D. H. Kim, S. H. Han, and J. S. Suh, "Overcoming artifacts from metallic orthopedic implants at high-field-strength MR imaging and multi-detector CT," Radiographics **27**(3), 791–803 (2007).
[108]K. M. Koch, J. E. Lorbiecki, R. S. Hinks, and K. F. King, "A multispectral three-dimensional acquisition technique for imaging near metal implants," Magn. Reson. Med. **61**(2), 381–390 (2009).
[109]I. A. Burger, M. C. Wurnig, A. S. Becker, D. Kenkel, G. Delso, P. Veit-Haibach, and A. Boss, "Hybrid PET/MR imaging: An algorithm to reduce metal artifacts from dental implants in Dixon-based attenuation map generation using a multiacquisition variable-resonance image combination sequence," J. Nucl. Med. **56**(1), 93–97 (2015).
[110]J. M. Gunzinger, G. Delso, A. Boss, M. Porto, H. Davison, G. K. von Schulthess, M. Huellner, P. Stolzmann, P. Veit-Haibach, and I. A. Burger, "Metal artifact reduction in patients with dental implants using multispectral three-dimensional data acquisition for hybrid PET/MRI," EJNMMI Phys. **1**(1), 102–115 (2014).
[111]T. Pan and H. Zaidi, "Attenuation correction strategies for positron emission tomography/computed tomography and 4-dimensional positron emission tomography/computed tomography," PET Clin. **8**(1), 37–50 (2013).
[112]C. Buerger, A. Aitken, C. Tsoumpas, A. P. King, V. Schulz, P. Marsden, and T. Schaeffter, "Investigation of 4D PET attenuation correction using ultra-short echo time MR," in *IEEE Nuclear Science Symposium and Medical Imaging Conference (NSS/MIC)* (IEEE, Valencia, Spain, 2011), pp. 3558–3561.
[113]H. Fayad, H. Schmidt, C. Wuerslin, and D. Visvikis, "4D attenuation map generation in PET/MR imaging using 4D PET derived motion fields," in *IEEE Nuclear Science Symposium and Medical Imaging Conference (NSS/MIC)* (IEEE, Seoul, Korea, 2013), pp. 1–4.
[114]A. Mehranian and H. Zaidi, "Emission-based estimation of lung attenuation coefficients for attenuation correction in PET/MR," Phys. Med. Biol. **60**(12), 4813–4833 (2015).
[115]A. Rezaei and J. Nuyts, "Joint registration of attenuation and activity images in gated TOF-PET," in *IEEE Nuclear Science Symposium and Medical Imaging Conference (NSS/MIC)* (IEEE, Seoul, Korea, 2013), pp. 1–4.
[116]L. R. MacDonald, S. Kohlmyer, C. Liu, T. K. Lewellen, and P. E. Kinahan, "Effects of MR surface coils on PET quantification," Med. Phys. **38**(6), 2948–2956 (2011).
[117]R. Kartmann, D. H. Paulus, H. Braun, B. Aklan, S. Ziegler, B. K. Navalpakkam, M. Lentschig, and H. H. Quick, "Integrated PET/MR imaging: Automatic attenuation correction of flexible RF coils," Med. Phys. **40**(8), 082301 (14pp.) (2013).
[118]S. Fürst, M. Souvatzoglou, A. Martinez-Moller, M. Schwaiger, S. G. Nekolla, and S. I. Ziegler, "Impact of flexible body surface coil and patient table on PET quantification and image quality in integrated PET/MR," Nuklearmedizin **53**(3), 79–87 (2014).
[119]G. Delso, A. Martinez-Möller, R. A. Bundschuh, R. Ladebeck, Y. Candidus, D. Faul, and S. I. Ziegler, "Evaluation of the attenuation properties of MR equipment for its use in a whole-body PET/MR scanner," Phys. Med. Biol. **55**(15), 4361–4374 (2010).
[120]B. Aklan, D. H. Paulus, E. Wenkel, H. Braun, B. K. Navalpakkam, S. Ziegler, C. Geppert, E. E. Sigmund, A. Melsaether, and H. H. Quick, "Toward simultaneous PET/MR breast imaging: Systematic evaluation and integration of a radiofrequency breast coil," Med. Phys. **40**(2), 024301 (11pp.) (2013).
[121]B. Zhang, D. Pal, Z. Hu, N. Ojha, G. Muswick, C.-H. Tung, and J. Kaste, "Attenuation correction for MR table and coils for a sequential

PET/MR system," in *IEEE Nuclear Science Symposium and Medical Imaging Conference*, *Orlando, FL, 25-31 October 2009* (IEEE, Orlando, FL, 2009), pp. 3303–3306.
[122]D. H. Paulus, L. Tellmann, and H. H. Quick, "Towards improved hardware component attenuation correction in PET/MR hybrid imaging," Phys. Med. Biol. **58**(22), 8021–8040 (2013).
[123]D. H. Paulus, H. Braun, B. Aklan, and H. H. Quick, "Simultaneous PET/MR imaging: MR-based attenuation correction of local radiofrequency surface coils," Med. Phys. **39**(7), 4306–4315 (2012).
[124]M. Eldib, J. Bini, C. Calcagno, P. M. Robson, V. Mani, and Z. A. Fayad, "Attenuation correction for flexible magnetic resonance coils in combined magnetic resonance/positron emission tomography imaging," Invest. Radiol. **49**(2), 63–69 (2014).
[125]S. Saha, "Whole body RF coil design for a simultaneous PET-MR system," *Joint Annual Meeting ISMRM-ESMRMB*, *Milan, Italy*, *2014*.
[126]I. Dregely, T. Lanz, S. Metz, M. F. Mueller, M. Kuschan, M. Nimbalkar, R. A. Bundschuh, S. I. Ziegler, A. Haase, S. G. Nekolla, and M. Schwaiger, "A 16-channel MR coil for simultaneous PET/MR imaging in breast cancer," Eur. Radiol. **25**(4), 1154–1161 (2015).
[127]M. Hofmann, B. Schölkopf, I. Bezrukov, and N. D. Cahill, "Incorporating prior knowledge on class probabilities into local similarity measures for intermodality image registration," *Proceedings of the MICCAI, Workshop on Probabilistic Models for Medical Image Analysis (PMMIA)*, *2009*.
[128]R. Karimi, G. Tornling, H. Forsslund, M. Mikko, A. Wheelock, S. Nyren, and C. M. Skold, "Lung density on high resolution computer tomography (HRCT) reflects degree of inflammation in smokers," Respir. Res. **15**, 23–32 (2014).
[129]J. H. Kim, J. S. Lee, I. C. Song, and D. S. Lee, "Comparison of segmentation-based attenuation correction methods for PET/MRI: Evaluation of bone and liver standardized uptake value with oncologic PET/CT data," J. Nucl. Med. **53**(12), 1878–1882 (2012).
[130]H. R. Marshall, F. S. Prato, L. Deans, J. Théberge, R. T. Thompson, and R. Z. Stodilka, "Variable lung density consideration in attenuation correction of whole-body PET/MRI," J. Nucl. Med. **53**(6), 977–984 (2012).
[131]A. R. Lonn and S. D. Wollenweber, "Estimation of mean lung attenuation for use in generating PET attenuation maps," in *IEEE Nuclear Science Symposium and Medical Imaging Conference (NSS/MIC)* (IEEE, Anaheim, CA, 2012), pp. 3017–3018.
[132]Y. Berker, A. Salomon, F. Kiessling, and V. Schulz, "Lung attenuation coefficient estimation using maximum likelihood reconstruction of attenuation and activity for PET/MR attenuation correction," in *IEEE Nuclear Science Symposium and Medical Imaging Conference (NSS/MIC)* (IEEE, Anaheim, CA, 2012), pp. 2282–2284.
[133]P. J. Schleyer, T. Schaeffter, and P. K. Marsden, "The effect of inaccurate bone attenuation coefficient and segmentation on reconstructed PET images," Nucl. Med. Commun. **31**(8), 708–716 (2010).
[134]B. K. Navalpakkam, H. Braun, T. Kuwert, and H. H. Quick, "Magnetic resonance-based attenuation correction for PET/MR hybrid imaging using continuous valued attenuation maps," Invest. Radiol. **48**(5), 323–332 (2013).
[135]W. Lee, J.-A. Park, K. M. Kim, I.-O. Ko, I. Lim, J. S. Kim, J. Kim, S.-K. Woo, J. h. Kang, and S. M. Lim, "Effects of MR contrast agents on PET quantitation in PET-MRI study [abstract]," J. Nucl. Med. **52**, 53 (2011).
[136]C. Lois, I. Bezrukov, H. Schmidt, N. Schwenzer, M. Werner, J. Kupferschläger, and T. Beyer, "Effect of MR contrast agents on quantitative accuracy of PET in combined whole-body PET/MR imaging," Eur. J. Nucl. Med. Mol. Imaging **39**(11), 1756–1766 (2012).
[137]S. Ahn, L. Cheng, and R. M. Manjeshwar, "Analysis of the effects of errors in attenuation maps on PET quantitation in TOF PET," *IEEE Nuclear Science Symposium Conference Record (NSS/MIC)*, *Seattle, WA*, *2014*.
[138]S. Wollenweber, G. Delso, T. Deller, D. Goldhaber, M. Hüllner, and P. Veit-Haibach, "Characterization of the impact to PET quantification and image quality of an anterior array surface coil for PET/MR imaging," Magn. Reson. Mater. Phys., Biol. Med. **27**(2), 149–159 (2014).
[139]H. Davison, E. E. Ter Voert, F. de Galiza Barbosa, P. Veit-Haibach, and G. Delso, "Incorporation of time-of-flight information reduces metal artifacts in simultaneous positron emission tomography/magnetic resonance imaging: A simulation study," Invest. Radiol. **50**(7), 423–429 (2015).
[140]T. W. Deller, A. M. Grant, M. M. Khalighi, S. H. Maramraju, G. Delso, and C. S. Levin, "PET NEMA performance measurements for a SiPM-based time-of-flight PET/MR system," *IEEE Nuclear Science Symposium and Medical Imaging Conference (NSS/MIC)*, *Seattle, WA*, *8–15 November 2014*.
[141]E. ter Voert, G. Delso, S. Ahn, F. Wiesinger, M. Huellner, and P. Veit-Haibach, "The effect of TOF on PET reconstructions in patients with (metal) implants in simultaneous TOF PET/MR scanning," in *Radiological Society of North America Scientific Assembly and Annual Meeting*, *Chicago, IL* (2014), p. SSK18-06.
[142]A. Mehranian and H. Zaidi, "Impact of time-of-flight PET on quantification errors in MRI-based attenuation correction," J. Nucl. Med. **56**(4), 635–641 (2015).
[143]K. G. Hollingsworth, "Reducing acquisition time in clinical MRI by data undersampling and compressed sensing reconstruction," Phys. Med. Biol. **60**(21), R297–R322 (2015).
[144]C. Li, J. Magland, and F. Wehrli, "Compressed sensing 3D ultrashort echo time (COMPUTE) imaging," *Proceedings of the 20th Annual Meeting of ISMRM*, *2012*.
[145]L. Hu, K.-H. Su, G. C. Pereira, A. Grover, B. Traughber, M. Traughber, and R. F. Muzic, "k-space sampling optimization for ultrashort TE imaging of cortical bone: Applications in radiation therapy planning and MR-based PET attenuation correction," Med. Phys. **41**(10), 102301 (9pp.) (2014).
[146]R. Galea, R. G. Wells, C. K. Ross, J. Lockwood, K. Moore, J. T. Harvey, and G. H. Isensee, "A comparison of rat SPECT images obtained using ^{99m}Tc derived from ^{99}Mo produced by an electron accelerator with that from a reactor," Phys. Med. Biol. **58**(9), 2737–2750 (2013).
[147]M. Weiger, D. O. Brunner, B. E. Dietrich, C. F. Muller, and K. P. Pruessmann, "ZTE imaging in humans," Magn. Reson. Med. **70**(2), 328–332 (2013).
[148]F. Wiesinger, L. I. Sacolick, A. Menini, S. S. Kaushik, S. Ahn, P. Veit-Haibach, G. Delso, and D. D. Shanbhag, "Zero TE MR bone imaging in the head," Magn. Reson. Med. **75**, 107–114 (2015).
[149]G. Delso, F. Wiesinger, L. I. Sacolick, S. S. Kaushik, D. D. Shanbhag, M. Hüllner, and P. Veit-Haibach, "Clinical evaluation of zero-echo-time MR imaging for the segmentation of the skull," J. Nucl. Med. **56**(3), 417–422 (2015).
[150]F. Gibiino, L. Sacolick, A. Menini, L. Landini, and F. Wiesinger, "Free-breathing, zero-TE MR lung imaging," Magn. Reson. Mater. Phys., Biol. Med. **28**(3), 207–215 (2015).
[151]G. Delso, S. Fürst, B. Jakoby, R. Ladebeck, C. Ganter, S. G. Nekolla, M. Schwaiger, and S. I. Ziegler, "Performance measurements of the Siemens mMR integrated whole-body PET/MR scanner," J. Nucl. Med. **52**(12), 1914–1922 (2011).
[152]A. Drzezga, M. Souvatzoglou, M. Eiber, A. J. Beer, S. Furst, A. Martinez-Moller, S. G. Nekolla, S. Ziegler, C. Ganter, E. J. Rummeny, and M. Schwaiger, "First clinical experience with integrated whole-body PET/MR: Comparison to PET/CT in patients with oncologic diagnoses," J. Nucl. Med. **53**(6), 845–855 (2012).
[153]M. Becker and H. Zaidi, "Imaging in head and neck squamous cell carcinoma: The potential role of PET/MRI," Br. J. Radiol. **87**(1036), 20130677 (2014).
[154]J. Czernin, L. Ta, and K. Herrmann, "Does PET/MR imaging improve cancer assessments? Literature evidence from more than 900 patients," J. Nucl. Med. **55**(Suppl. 2), 59S–62S (2014).
[155]C. Spick, K. Herrmann, and J. Czernin, "^{18}F-FDG PET/CT and PET/MRI perform equally well in cancer patients: Evidence from studies in more than 2300 patients," J. Nucl. Med. **57**, 1–11 (2016).
[156]H. T. van Dam, G. Borghi, S. Seifert, and D. R. Schaart, "Sub-200 ps CRT in monolithic scintillator PET detectors using digital SiPM arrays and maximum likelihood interaction time estimation," Phys. Med. Biol. **58**(10), 3243–3257 (2013).
[157]K. Doroud, A. Rodriguez, M. C. S. Williams, K. Yamamoto, A. Zichichi, and R. Zuyeuski, "Systematic study of new types of Hamamatsu MPPCs read out with the NINO ASIC," Nucl. Instrum. Methods Phys. Res., Sect. A **753**, 149–153 (2014).
[158]J.-y. Cui, G. Pratx, S. Prevrhal, and C. S. Levin, "Fully 3D list-mode time-of-flight PET image reconstruction on GPUs using CUDA," Med. Phys. **38**(12), 6775–6786 (2011).
[159]I. Hong, W. Luk, V. Panin, C. Watson, F. Kehren, and M. Casey, "Real-time PET reconstruction," *IEEE Nuclear Science Symposium and Medical Imaging Conference (NSS/MIC)*, *Seattle, WA*, *8–15 November 2014*.
[160]A. Afshar-Oromieh, U. Haberkorn, H. P. Schlemmer, M. Fenchel, M. Eder, M. Eisenhut, B. A. Hadaschik, A. Kopp-Schneider, and M. Röthke,

"Comparison of PET/CT and PET/MRI hybrid systems using a ^{68}Ga-labelled PSMA ligand for the diagnosis of recurrent prostate cancer: Initial experience," Eur. J. Nucl. Med. Mol. Imaging **41**(5), 887–897 (2014).

[161]M. Covello, C. Cavaliere, M. Aiello, M. S. Cianelli, M. Mesolella, B. Iorio, A. Rossi, and E. Nicolai, "Simultaneous PET/MR head–neck cancer imaging: Preliminary clinical experience and multiparametric evaluation," Eur. J. Radiol. **84**(7), 1269–1276 (2015).

[162]S. Partovi, A. Kohan, J. L. Vercher-Conejero, C. Rubbert, S. Margevicius, M. D. Schluchter, C. Gaeta, P. Faulhaber, and M. R. Robbin, "Qualitative and quantitative performance of ^{18}F-FDG-PET/MRI versus ^{18}F-FDG-PET/CT in patients with head and neck cancer," Am. J. Neuroradiol. **35**(10), 1970–1975 (2014).

[163]A. Varoquaux, O. Rager, A. Poncet, B. M. Delattre, O. Ratib, C. D. Becker, P. Dulguerov, N. Dulguerov, H. Zaidi, and M. Becker, "Detection and quantification of focal uptake in head and neck tumours: ^{18}F-FDG PET/MR versus PET/CT," Eur. J. Nucl. Med. Mol. Imaging **41**(3), 462–475 (2014).

[164]S. I. Lee, O. A. Catalano, and F. Dehdashti, "Evaluation of gynecologic cancer with MR imaging, ^{18}F-FDG PET/CT, and PET/MR imaging," J. Nucl. Med. **56**(3), 436–443 (2015).

[165]D. A. Torigian, H. Zaidi, T. C. Kwee, B. Saboury, J. K. Udupa, Z.-H. Cho, and A. Alavi, "PET/MR imaging: Technical aspects and potential clinical applications," Radiology **267**(1), 26–44 (2013).

[166]J. Steinberg, G. Jia, S. Sammet, J. Zhang, N. Hall, and M. V. Knopp, "Three-region MRI-based whole-body attenuation correction for automated PET reconstruction," Nucl. Med. Biol. **37**(2), 227–235 (2010).

[167]J. H. Jonsson, M. M. Akhtari, M. G. Karlsson, A. Johansson, T. Asklund, and T. Nyholm, "Accuracy of inverse treatment planning on substitute CT images derived from MR data for brain lesions," Radiat. Oncol. **10**(1), 13–19 (2015).

[168]J. A. Dowling, J. Lambert, J. Parker, O. Salvado, J. Fripp, A. Capp, C. Wratten, J. W. Denham, and P. B. Greer, "An atlas-based electron density mapping method for magnetic resonance imaging (MRI)-alone treatment planning and adaptive MRI-based prostate radiation therapy," Int. J. Radiat. Oncol., Biol., Phys. **83**(1), e5–e11 (2012).